SANDIA REPORT

SAND2012-10389
Unlimited Release
December 2012

Development of a Raman Spectroscopy Technique to Detect Alternate Transportation Fuel Hydrocarbon Intermediates in Complex Combustion Environments

Isaac W. Ekoto
Robert S. Barlow

Prepared by
Sandia National Laboratories
Albuquerque, New Mexico 87185 and Livermore, California 94550

Sandia National Laboratories is a multi-program laboratory managed and operated by Sandia Corporation, a wholly owned subsidiary of Lockheed Martin Corporation, for the U.S. Department of Energy's National Nuclear Security Administration under contract DE-AC04-94AL85000.

Issued by Sandia National Laboratories, operated for the United States Department of Energy by Sandia Corporation.

Available to DOE and DOE contractors from
U.S. Department of Energy
Office of Scientific and Technical Information
P.O. Box 62
Oak Ridge, TN 37831

Telephone: (865) 576-8401
Facsimile: (865) 576-5728
E-Mail: reports@adonis.osti.gov
Online ordering: http://www.osti.gov/bridge

Available to the public from
U.S. Department of Commerce
National Technical Information Service
5285 Port Royal Rd.
Springfield, VA 22161

Telephone: (800) 553-6847
Facsimile: (703) 605-6900
E-Mail: orders@ntis.fedworld.gov
Online order: http://www.ntis.gov/help/ordermethods.asp?loc=7-4-0#online

SAND2012-10389
Unlimited Release
December 2012

Development of a Raman Spectroscopy Technique to Detect Alternate Transportation Fuel Hydrocarbon Intermediates in Complex Combustion Environments

Isaac W. Ekoto
Hydrogen and Combustion Technologies
Sandia National Laboratories
7011 East Avenue MS 9052
Livermore, CA. 94550

Robert S. Barlow
Reacting Flow Research
Sandia National Laboratories
7011 East Avenue MS 9051
Livermore, CA. 94550

Abstract

Spontaneous Raman spectra for important hydrocarbon fuels and combustion intermediates were recorded over a range of low-to-moderate flame temperatures using the multiscalar measurement facility located at Sandia/CA. Recorded spectra were extrapolated to higher flame temperatures and then converted into empirical spectral libraries that can readily be incorporated into existing post-processing analysis models that account for crosstalk from overlapping hydrocarbon channel signal. Performance testing of the developed libraries and reduction methods was conducted through an examination of results from well-characterized laminar reference flames, and was found to provide good agreement. The diagnostic development allows for temporally and spatially resolved flame measurements of speciated hydrocarbon concentrations whose parent is more chemically complex than methane. Such data are needed to validate increasingly complex flame simulations.

ACKNOWLEDGMENTS

The authors gratefully acknowledge Dirk Geyer from Hochschule Darmstadt and Frederik Fuest from The Ohio State University for their technical expertise and advice regarding the Raman spectra data interpretation, along with implementation and interpretation of the calculated spectral libraries from the RAMSES code. Furthermore, Matthew Dunn from the University of Sydney and Bob Harmon from Sandia National Laboratories are acknowledged for their tireless assistance with data acquisition and post-processing.

CONTENTS

FIGURES

TABLES

NOMENCLATURE

A	basis function model peak amplitude
D	molecular diffusion
g	gravitational body force [N]
u	velocity [m/s]
p	pressure [Pa]
h	specific enthalpy [m^2/s^2]
S	Raman signal vector
N	chemical species number density
P	Raman channel crosstalk matrix
T	temperature [K]
Y	mass fraction
J^s	chemical species flux
J^h	enthalpy flux
x	spatial scale [m]
t	time scale [s]
M	species molecular weight [g/mole]
$\dot{q}_r$	radiative heat flux
α	basis function model peak skewness
λ	thermal conductivity
μ	basis function model peak center location [nm]
ξ	mixture fraction
ρ	density [kg/m^3]
σ	Rayleigh cross-section
τ	viscous stress tensor
χ	scalar dissipation
ω	basis function model peak width

Subscripts/Superscripts:

0, 1	intercept and slope for the basis function linear fit
C	*carbon element*
H	*Hydrogen element*
eff	effective value
n	atomic element
ns	atomic element number per molecular species
i, j, k	Cartesian tensor notation spatial components
s	chemical species
Ray	Rayleigh

Acronyms:

CCD	Charge Coupled Device
DOE	Department of Energy
DME	Dimethyl Ether

DNS	Direct Numerical Simulation
FDF	Filtered Density Function
LES	Large Eddy Simulation
LIF	Laser Induced Fluorescence
PDF	Probability Density Function
SNL	Sandia National Laboratories
TNF	Turbulent Non-premixed Flame

1. INTRODUCTION

Sandia has heavily invested in novel production pathways for synthetic and biologically derived fuel types (e.g., Sunshine to Petrol and the Joint BioEnergy Institute) as a means of reducing greenhouse gas emissions. However, needed numerical combustion modeling within representative combustion devices has lagged, in part because of a lack of detailed experimental scalar and velocity data needed for phenomenological sub-model development and validation. A major diagnostic hurdle remains the inability to directly and quantifiably measure the concentrations of alternative hydrocarbon fuels and their stable combustion intermediates at suitable spatial and temporal scales required to resolve variables such as mixture fraction and scalar dissipation. The gap can be bridged by taking advantage of recent advances in efficient detection techniques for spontaneous Raman scattering and through the diagnostic developments described in this report. The challenge is to differentiate overlapping, temperature dependent Raman spectral signatures from hydrocarbon fuels and their combustion intermediates and then convert this information into accurate concentration measurements. Preliminary Raman scattering measurements from laboratory flames of dimethyl ether (DME) – a simple ether that is a promising diesel surrogate with favorable combustion and emission characteristics – indicate this separation is possible provided that detailed, temperature specific, information of the Raman spectral shift is known for the major intermediate hydrocarbon species along with the parent fuel.

1.1 Background

It has been well documented that closely coupled chemical and physical phenomena within turbulent flames control ignition processes, flame stability, and the formation of air quality emissions for most combustion driven power generation applications [1-3]. Cooperative experimental research on benchmark flame types through Turbulent Nonpremixed Flame (TNF) Workshops [4] has provided sorely needed validation data of novel phenomenological models [5-9] and high-fidelity numerical simulations [10-14]. Of particular relevance are *in-situ* measurements of temperature, major species, and mixture fraction obtained from point or line-imaged spontaneous Raman scattering of an incident high energy laser pulse [15-38]. Spontaneous Raman spectroscopy is a non-intrusive measurement of inelastic molecular light scattering where the light emission distribution, frequency shifted from the incident laser line, results from molecularly distinct differential polarizabilities and quantized energy states [39]. Raman scattering represents a discrete-sample system with an input function based on the *in situ* molecular distribution and incident laser light, and the emitted radiation spectrum as the output. The resulting Raman spectrum is thus species specific, linearly proportional to molecule number density, and a function of temperature since the initial energy state distribution itself is inherently temperature dependent. For such processes, the system input is mapped to the system output through a defined functional set [40], where determination of the unknown system input function relies solely on knowledge of the system output and the functional transformation inverse. Whether a system is invertible, and hence has a unique system transformation, strongly depends on the molecular distribution complexity and the fidelity of the signal recording methodology. The temperature dependence is usually accounted for through imaging of elastic (Rayleigh) molecular scattering. More recently, these Raman/Rayleigh scattering diagnostics, when combined with cross-plane OH laser induced fluorescence (LIF) imaging, have been extended to measure 3D reaction progress variable gradients required for much needed scalar dissipation measurements [33, 36].

For Raman scattering induced from visible wavelength laser sources, signal separation in spectral space between main product, non-fuel reactant, and intermediate species spectra (i.e., from CO_2, H_2O, N_2, O_2, CO, and H_2 Raman scattering signals) is sufficient such that signal cross-talk is manageable. However, due to exceedingly small differential cross-sections – constraints that necessitate large incident laser irradiances, sensitive photo detectors, and minimized spurious luminosity [41] – applications within optical combustion chambers have been limited to non-luminous [41] or non-reacting [37] environments. To reduce photo-fluorescence and incandescence interferences the impact of ultraviolet (UV) excitation has been explored [19, 24, 29, 30]. However, luminosity interference reductions are often outweighed by reduced laser fluences and photo-detector quantum efficiencies at the lower wavelengths. Hence most researchers instead choose a visible excitation wavelength and monitor an interference channel to account for potential C_2 LIF [15, 28]. For sooty flames, some researchers have taken advantage of the fact that unlike incandescence and fluorescence interference sources, Raman scattered light has very little depolarization from the incident light source. Separation techniques have been developed whereby both the parallel (p) and perpendicular (s) polarization components are simultaneously recorded, with the unfiltered incandescence/fluorescence removed using detailed information about the Raman emission spectrum depolarization ratio [42, 43].

Matrix inversion and spectral fitting methods have traditionally been used to quantify species concentrations from the measured signal [38]. For the matrix inversion approach, recorded signals are integrated across fixed spectral regions to create a signal vector, *S*, with an element number equal to the species number densities, *N*, and the vectors related through the temperature dependent Raman response matrix, *P*.

$$S = P(T)N \tag{1.1}$$

In equation 1.1, the diagonal elements of *P* represent the principal integrated signal component for each species, while off-diagonal elements represent crosstalk due to overlap of Raman scattering spectra from different species as well as signal contributions from chemiluminescence and laser induced fluorescence of C_2 and various hydrocarbon soot precursors. The Raman response matrix is calibrated using measurements from heated gases and well-characterized reference laminar flames. Temperature dependence is accounted for from the measured effective Rayleigh differential cross-section determined from the Rayleigh signal and using known Rayleigh differential cross-sections for each chemical species:

$$\sigma_{Ray,eff} = \Sigma_i X_i \sigma_{Ray,i} \tag{1.2}$$

Recursive methods are used to iteratively converge temperature and species concentration until a best fit condition is achieved between both the Rayleigh and Raman measurements. While the matrix inversion method can be rapidly processed and on-chip binning minimizes readout noise, spectral broadening and shifts due to shot-to-shot input laser beam profile fluctuations can result in lost information. Moreover, large calibration uncertainties can lead to poor concentration measurement resolution for certain species within a range of temperatures.

Alternatively, a spectral fit approach has been developed where theoretical spectral libraries are generated from calculated, temperature dependent, Raman transitions (e.g., RAMSES [44])

and convolved with the experiment apparatus function to reproduce the target spectra. Signal calibrations from samples at known concentrations and temperatures are used to verify library reliability. The measured signal power spectrum is estimated from harmonic methods that take advantage of the orthogonality of noise and signal subspaces, while the local flame temperature is once again determined from Rayleigh scatter measurements and is used to create reference spectra from the calculated libraries. Transformation power spectral functions are derived from cross-correlations between reference and measured spectra, and recursive methods are used to calculate temperature and species concentrations. The spectral fitting approach has the advantage that it limits the number of calibrations to the number of species investigated and has lower uncertainties at moderate to high flame temperatures relative to direct calibrations from reference flames. However, slow data acquisition rates, elevated readout noise, and signal modeling complexity can make this method impractical.

More recently, these reduction techniques have been combined into the so-called hybrid method where on-chip binning and signal vectors from the matrix inversion method are preserved, while the extensive calibrations are replaced by calculated spectral libraries convolved with apparatus transfer functions [38]. The hybrid method coupled with advanced wavelet denoising techniques has yielded detection limits (mean signal equals noise) well below 1% mole fraction at flame temperatures for Raman measurements in the Sandia/CA facility.

When accounting for hydrocarbon signal contributions, Barlow et al. [25] demonstrated that for methane fueled flames overlapping C–H bond stretch spectra from hydrocarbon intermediates was negligible and could be accounted for through the use of appropriate calibration corrections. With more complex hydrocarbon fuel types, this advantageous situation does not exist as overlapping spectral contributions from hydrocarbon intermediates become non-negligible. Moreover, C–C Raman spectra contributions that overlap CO_2 and O_2 channels must now be considered. Accordingly, few reported studies exist of line imaged Raman spectroscopy applied to flames fueled by complex hydrocarbons. For those that do [16, 17, 29, 30], compromises in signal-to-noise were made from non-optimal line selection or overly lean mixtures near the global extinction limits were used to minimize fluorescence and incandescence interferences. Recently acquired C–H bond stretch Raman spectra from premixed DME flames appear to be sufficiently distinct such that unique signal decomposition can be achieved [38]. To perform the separation, detailed information about the Raman spectra and the corresponding temperature response are needed; information that to date is only available at atmospheric temperature and pressures (e.g., Stephenson [45]).

1.2 Objective

The project objective was to extend Raman spectroscopy as a combustion diagnostic such that *in situ* hydrocarbon concentrations can be quantified. To achieve this objective, empirical Raman spectral libraries were developed for the primary stable combustion intermediates and the parent fuel in these flames over a broad range of relevant flame temperatures using Sandia/CA's multiscalar measurement facility. These spectra were recorded from room temperatures up to ~900 K in 100 K increments, with temperature dependent empirical spectra generated through the use of a novel signal decomposition routine that separated the measured signal into basis functions. Model spectra were formed by the extrapolation of basis values to the target temperature where the signal could then be reconstructed. To develop libraries that could be used

for polarization separation techniques, both perpendicular and parallel polarization filtered scattering spectra were recorded, along with the unfiltered spectra. Performance testing was carried out by comparing empirical spectra to measured spectra from well-characterized laminar flame data.

The current report discusses the experimental development of these empirical spectral libraries along with the results of performance validation under well-characterized DME flames. The report is structured as follows: Section 1 summarizes the current state of spontaneous Raman spectroscopy as a flame diagnostic and outlines the research objectives and approach. Section 2 provides a brief discussion of the theoretical framework along with detailed descriptions of the combined experimental and modeling approach used to generate the spectral libraries. Measured spectral libraries for low to moderate flame temperatures ($T < 900$ K) are presented in Section 3 along with extrapolations to higher temperatures, while an evaluation of the performance of these libraries from heated mixtures of arbitrary composition and well-characterized laminar flames is presented in Section 4. A results summary with important conclusions is given in Section 5, and developed libraries are cataloged in Appendix A.

2. EXPERIMENTAL SETUP

2.1 Theoretical Framework

To establish a consistent notation and clearly identify combustion variables that require validation measurements the governing equations for chemically reacting turbulent flows are reviewed here. The differential form for the mass, momentum, energy and chemical species conservation equations (Y_s: $\Sigma Y_s = 1$) are expressed below in tensor notation, where subscripts *i*, *j*, and *k* denote the components of the three-dimensional Cartesian vector:

2.1 $$\frac{\partial \rho}{\partial t} + \frac{\partial \rho u_i}{\partial x_i} = 0$$

2.2 $$\frac{\partial \rho u_j}{\partial t} + \frac{\partial \rho u_j u_i}{\partial x_i} + \frac{\partial p}{\partial x_j} - \frac{\partial \tau_{ij}}{\partial x_i} = \rho g_j; \quad \tau_{ij} = -\mu\left(\frac{\partial u_i}{\partial x_j} + \frac{\partial u_j}{\partial x_i} - \frac{2}{3}\frac{\partial u_i}{\partial x_i}\delta_{ij}\right)$$

2.3 $$\frac{\partial \rho h}{\partial t} + \frac{\partial \rho h u_i}{\partial x_i} + \frac{\partial J_i^h}{\partial x_i} - \frac{\partial p}{\partial t} - \frac{\partial p u_i}{\partial x_i} - \tau_{ij}\frac{\partial u_j}{\partial x_i} = \dot{q}_r; \quad J_i^h \approx -\lambda\frac{\partial T}{\partial x_i}$$

2.4 $$\frac{\partial \rho Y_s}{\partial t} + \frac{\partial \rho Y_s u_i}{\partial x_i} + \frac{\partial J_i^s}{\partial x_i} = M_s\frac{\partial Y_s}{\partial t}; \quad J_i^s \approx -D\rho\frac{\partial Y_s}{\partial x_i}$$

Here the terms *u*, ρ, *p*, and *h* respectively represent the convective velocity along with the state variables density, pressure and enthalpy. The term M_s represents the species specific molecular weight, *g* is the gravitational body force, and $\dot{q}_r$ is the radiative heat flux. The quantities τ, J^s, and J^h, represent the viscous stress tensor and the fluxes of species and enthalpy respectively. Here, the fluid is assumed to be Newtonian with a dynamic viscosity μ, and with mixture averaged diffusion and thermal conductivity coefficients, *D* and λ. The assumption of a mixture averaged molecular diffusion is often poor as different species diffuse at different rates – hydrogen in particular – but is commonly adopted to reduce computational constraints and model complexity. Pressure and thermal diffusion terms were neglected as second order from the species molecular flux, while only the contribution from heat conduction was considered for the enthalpy flux term.

Turbulent combustion is a vastly complex process that involves closely coupled flow physics and reaction chemistry over a broad range of temporal and spatial scales. Equations 2.1 – 2.4 are sufficient to determine the spatial evolution of all mixture dependent variables provided appropriate initial and boundary conditions are specified. However, turbulent combustion direct numerical simulation (DNS), even for simple applications, far outpaces most available computational resources. Furthermore, even if the complete data set could be determined, such a level of detail is much greater than what is generally needed for computational based combustion system design. For such systems, key outputs such as fuel consumption, power generation, and pollutant formation are often needed on a globally averaged basis. Reduced order phenomenological models are thus needed to relax the resolution requirements, while still sufficiently predicting the global quantities of interest. A common approach that allows for easier data interpretation and insight into the physical/chemical phenomena is to only consider temporally averaged forms of the governing equations, which results in additional terms that require models to close the system of equations. Experimental validation data from resolved model variable probability density functions (PDFs) are needed to verify model applicability.

Several methods exist to achieve model closure for the averaged form of equations 2.1 – 2.3, but a discussion of these approaches is beyond the scope of this report; for more information the reader is referred to references [46-48]. The treatment of equation 2.4 is a bit more complex as the number of reactions and species within a realistic system can number in the thousands, and the quantities are not conserved due to the presence of a source term. Thus, it makes sense to express species conservation in terms of element conservation equations, which eliminates the need for source terms and dramatically reduces the number of variables that need to be considered [49]. The elemental mass fractions are thus defined as:

$$2.5 \qquad Y_n = \sum_{s=1} N_{sn} \frac{M_n}{M_s} Y_s$$

where N_{sn} is the number of atomic elements n within each molecular species s and M_n represents the element molar mass. Further simplification can be achieved by assuming equal species diffusivity as was done in equation 2.4 and expressing the element mass fractions in terms of a conserved scalar mixing variable, the mixture fraction ξ:

$$2.6 \qquad \xi = \frac{Y_n - Y_{n2}}{Y_{n1} - Y_{n2}}$$

Here, subscripts 1 and 2 represent the fuel and oxidizer streams respectively. A more complex definition by Bilger et al. [50] is widely used to model hydrocarbon flames because it better tracks reaction progress and preserves the stoichiometric mixture fraction value independent of the effects of differential diffusion:

$$2.7 \qquad \xi = \frac{2Y_C/M_c + Y_H/2M_H + (Y_{O,2} - Y_O)/M_O}{2Y_{C,1}/M_c + Y_{H,1}/2M_H + Y_{O,2}/M_O}$$

Here, the subscripts *C*, *H*, and *O* represent elemental carbon, hydrogen, and oxygen respectively.

For flames with reaction rates in chemical equilibrium – i.e., chemical kinetics are overly fast relative to mixing rates and heat loss – equation 2.4 can be represented purely as a function of the mixture fraction:

$$2.8 \qquad \frac{\partial \rho \xi}{\partial t} + \frac{\partial \rho \xi u_i}{\partial x_i} - \frac{\partial}{\partial x_i}\left(D\rho \frac{\partial \xi}{\partial x_i}\right) = 0$$

If the fast chemistry assumption is relaxed, the chemical source term can no longer be neglected and the system will accordingly move away from equilibrium as the mixing rate becomes more dominant. A parameter is needed to characterize this departure from equilibrium and the laminar flamelet concept is commonly invoked [49]. For the flamelet approach, the rate controlling processes are driven by local convective and chemical scales. Ultimately, the range of possible solutions for a given mixture composition is bounded by the equilibrium solution and the extinction limit. Intuitively this suggests overall reaction rates should then also be a function of the mixture fraction gradient and molecular diffusion. This assumption can be demonstrated explicitly by reevaluating equation 2.4 with the assumption that each chemical species is only a function of the mixture fraction, i.e., $Y_s(\xi)$. Equation 2.4 can then be expressed as:

$$2.9 \quad \frac{\partial Y_s}{\partial \xi}\left[\frac{\partial \rho \xi}{\partial t} + \frac{\partial \rho \xi u_i}{\partial x_i} - \frac{\partial}{\partial x_i}\left(D\rho \frac{\partial \xi}{\partial x_i}\right)\right] - \frac{1}{2}\rho\chi \frac{\partial^2 Y_s}{\partial \xi^2} = M_s \frac{\partial Y_s}{\partial t}$$

where, χ is commonly referred to as the scalar dissipation and defined as:

$$2.10 \quad \chi \equiv 2D\left(\frac{\partial \xi}{\partial x_i}\right)^2$$

Substitution of equation 2.8 into 2.9 produces:

$$2.11 \quad -\frac{1}{2}\rho\chi \frac{\partial^2 Y_s}{\partial \xi^2} = M_s \frac{\partial Y_s}{\partial t}$$

Thus, the rate of overall species consumption/formation relies on mixture fraction and scalar dissipation as reaction progress variables. Accordingly model formulations are based on these terms and require high-fidelity data sets to be properly validated.

An alternative to the fully probabilistic approach is the use of filtered density function (FDF) [51-54] to reduce the wide dynamic range of scales inherent to high Reynolds number turbulent combustion, which is a basis for large eddy simulation (LES). In LES, the dynamics of resolved scales, those larger than a prescribed filter width, are explicitly determined while the smaller fluctuations are modeled via the FDF. Recent reviews [55-57] have documented the advantages LES has over probabilistic approaches for simulations of laboratory flames along with gas-turbine and reciprocating engine combustion applications. However, since the essential rate limiting processes for chemically reacting turbulent flows occur at the unresolved scales, the model treatment of species conservation is similar to the flamelet approach outlined above [52]. A fuller description of the model formulation is beyond the scope of this document, and the reader is referred to more detailed reviews [58, 59].

2.2 Multiscalar Measurement Facility

The Sandia multiscalar facility (see Figure 1) has well-documented capabilities for simultaneous line imaging of spontaneous Raman and Rayleigh scatter to quantify *in situ* temperature and major species concentrations (CO_2, O_2, CO, N_2, CH_4, H_2O, and H_2) within methane and/or hydrogen fueled flames [36, 60]. To maximize the spontaneous Raman signal, four frequency-doubled Nd:YAG lasers with a total delivered energy of up to 1.8 J/pulse were focused into a 6 mm long probe volume with an interrogation region beam diameter of ~220 µm ($1/e^2$). Because of the high laser fluences, the timing of each ~9 ns laser pulse was offset 100 ns and optical delay lines were used to temporally stretch the pulses to minimize photo-fragmentation fluorescence interferences. The facility has additional capabilities of line imaged CO LIF to improve the CO measurement fidelity and cross-planar OH LIF to characterize 3D mixture fraction gradients used to calculate scalar dissipation. For the present study, however, neither the CO nor the OH LIF measurements were performed as these were not needed to describe the hydrocarbon rovibrational Raman stretch spectrum.

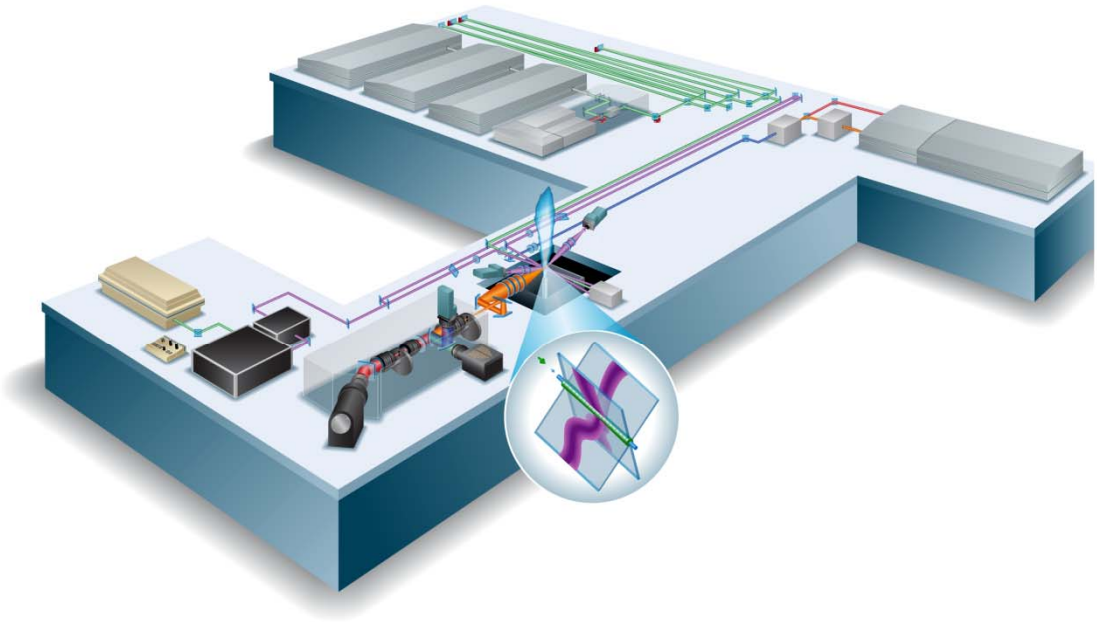

Figure 1. Schematic of the multiscalar measurement facility located at the Combustion Research Facility in Sandia/CA.

Raman and Rayleigh scatter were imaged by a single detection unit that housed two non-intensified, low-noise, CCD cameras for separate detection of the Raman and Rayleigh signals. A Princeton Instruments VersArray 1300B CCD camera that was cryogenically-cooled by a CryoTiger cooling unit (163 K) was used to detect the Raman signal. The detection unit contained a pair of custom 150 mm achromatic lenses (Linos Photonics, f = 300 mm, f/2 and f/4) that focused each camera along the full length of the 6 mm long probe volume. Spectral separation of elastic (532 nm) and inelastic shifted scatter (~930 – 4300 cm^{-1}) was achieved through the use of a long pass beam splitter, where a 10 nm (FWHM) band-pass filter was used to further isolate the Rayleigh scatter and a custom holographic Kaiser Optical transmission grating with high optical throughput was used to image the Raman spectrum. Spurious luminosity was minimized through the use of two custom-built optical chopper wheels that provided 3.9 µs (FWHM) mechanical gating for the Raman camera. Three polarization conditions were examined – parallel (p), perpendicular (s), or unfiltered – by placing the appropriate filter in front of the Raman camera. Object Rayleigh image plane pixel resolution was 19.4 µm after 2×2 hardware binning was applied. Raman spectra were acquired using the full camera spectral resolution (~0.12 nm/pixel), while the spatial resolution for the Raman line images was either 100 or 200 µm depending on whether 10 or 20 pixel spatial axis hardware binning was performed. This spatial binning resulted in either 30 or 60 strips of spectral

information. A common alignment plane was established by independently focusing each camera to a back illuminated target with a linear pattern of 50 μm laser drilled holes at the object plane.

2.3 Gas Heater

A custom designed electric gas heater assembly was used to generate heated hydrocarbon gas samples. To reduce the chance for unwanted ignition as the gas samples entrained ambient air once outside of the assembly, each sample was diluted by nitrogen (80% by volume) prior to entering the heater assembly. A total 25 lit/min flow rate was achieved via MKS and Tescom flow controllers that were calibrated by laminar flow elements to within 1% of the target flow rate. The heater assembly, a schematic is displayed in Figure 2 along with an image when in operation, consisted of a 0.635 m long quartz tube with a 30.1 mm outer diameter at the outlet and a wall thickness of 1.5 mm. At the tube base was a 38.7 mm in diameter flanged quartz piece. Four smaller quartz tubes that were 8.9 cm in length and had a 9.5 mm outer diameter were placed along the side of the main quartz tube. The two lower tubes were placed at opposite heights approximately 5.1 cm up from the flanged base, and were used as the inlet for the gas mixtures. Two additional ports were located 45.7 and 50.8 cm respectively above the base on opposite sides. One port was capped (the lower of the two), while the higher port was used to place a type-K thermocouple into gas stream to monitor the gas temperature near the exit.

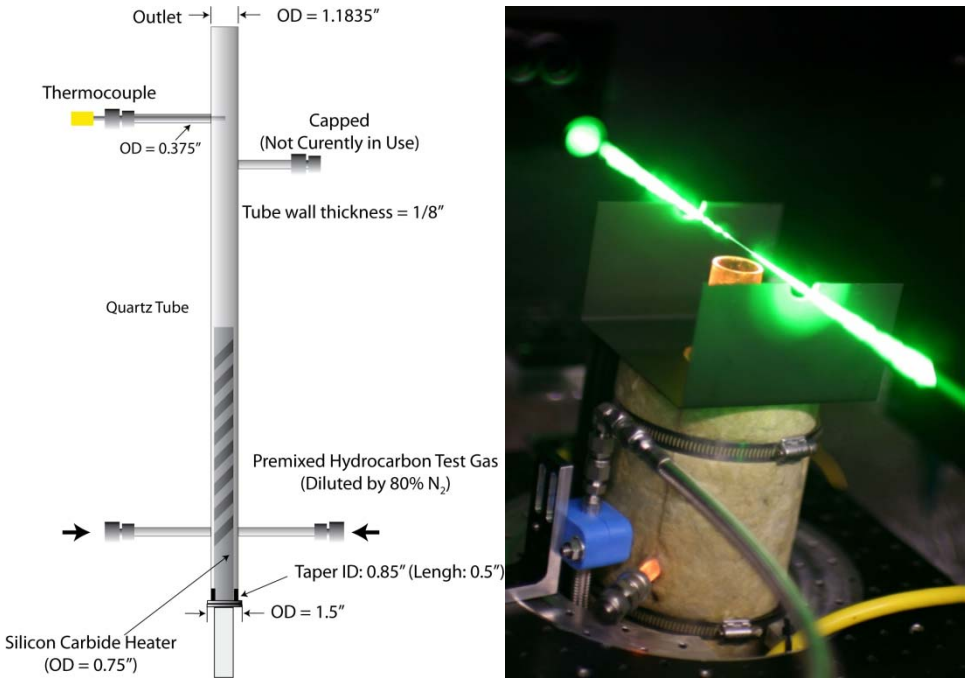

Figure 2. Schematic of the quartz tube gas heater assembly and silicon carbide heater, along with an image of the assembly during the Raman/Rayleigh measurements of N_2 diluted heated hydrocarbons.

Gas samples were heated via an I Squared R SER320x210x19 mm double spiral heat zone silicon carbide heater element that was 32 cm long with 21 cm of heating length and 19 mm in diameter. The element was seated against the quartz tube flanged base via a custom clamp assembly designed to minimize mechanical stresses on the quartz body. Heat loss from the

quartz tube was minimized by surrounding the entire assembly with two inch thick fiberglass insulation material. Power to the heater element was supplied by a Variac variable transformer, with the supplied current manually adjusted until the desired temperature was reached and remained steady according to real-time meter readouts from the tube thermocouple. Overall heater element impedance was 5.39 ohms, which enabled heating the gas samples in 100 K increments from room temperature (291 K) up to ~900 K – higher temperatures were not possible due to heater element off-gassing that led to interference in the Raman/Rayleigh measurements. Spectra at more representative flame temperatures were created from a newly developed spectral extrapolation technique; more details are provided in Section 3.

During the experiments, the outlet of the gas heater assembly was raised as close to the laser beam as possible so that there would be no air entrainment within the 6 mm long laser probe volume. Custom baffles that were painted black were placed around the heater element to minimize backscatter from the incident laser light. Total pulse energies during the experiments were reduced to 0.8 J/pulse for most hydrocarbon gases to minimize photo-fragmentation interferences. For C_2H_2 and C_2H_4 gas samples that were more sensitive to photo-fragmentation, total pulse energies were reduced until fluorescence interferences were eliminated (0.1 and 0.4 J/pulse respectively).

2.4 Laminar Vertical Flame & CHEMKIN PRO Simulations

To evaluate the performance of developed spectral libraries, a reference laminar flame was selected as a test case. The test flame was produced from a 50 mm diameter premixed laminar flow burner, tilted 30°, and with a rod mounted such that the main leg of a stabilized V-flame was vertical and normal to the incident laser axis (see Figure 3). Two fuel types were evaluated: a premixed CH_4/air flame (φ = 0.67) with a 64.2 L/min total flow rate and a premixed DME/air flame (φ = 0.66) with a 52.3 L/min total flow rate. A 70 L/min nitrogen co-flow was used to limit the impact of spurious room currents, although the annular coflow assembly is not shown in the photograph.

	Gas [L/min]	Air [L/min]	ϕ
CH4	4.2	60	0.67
DME	2.3	50	0.66

Figure 3. Tilted (30°) laminar flow burner with a stabilizing rod to produce nearly vertical and planar CH_4 and DME flames.

3. EMPIRICAL SPECTRAL LIBRARIES

Empirical spectral libraries were generated from heated gas measurements acquired in the multiscalar measurement facility as described in Section 2. The present section discusses the data post-processing used to develop the empirical spectra, including corrections for laser power and background, filters for dust particle and fluorescence interferences, noise reduction strategies, and conditional averages for corrected samples. The section concludes with a discussion of the additional post-processing applied for the vertical premixed flame data.

3.1 Data Post Processing

As described in Section 2, the spectra from 6 heated hydrocarbon gases volume diluted 80% by N_2 along with a pure N_2 flow were recorded in ~100 K increments from room temperature up to ~900 K at 3 polarization conditions. For each of the 21 conditions, 100 simultaneous Raman and Rayleigh images were recorded along with the corresponding laser pulse energy and ambient temperature/pressure conditions. Raman spectra were acquired using full spectral resolution of the camera (~0.12 nm/pixel) with 200 μm hardware binning in the spatial direction (20 pixels) on the center 2 mm portion of the 6 mm probe volume for 10 strips of data overall. The entire probe volume was imaged by the Rayleigh camera (340×45 pixels), however, only Rayleigh data that corresponded to the central 2 mm of the probe volume was considered.

At the start of each day and at multiple times throughout the day the laser system was shuttered and the camera system was used to record 100 background images from both the Rayleigh and Raman cameras. During post-processing, corresponding background images were averaged and then subtracted from the intensity counts of the respective spectral images. To further guard against a shift in background counts throughout the day, Raman spectra between pixels 1000 to 1250 were averaged and subtracted from the entire signal as there was essentially no spectral response in this region from either the hydrocarbon or nitrogen spectra. After background subtraction, individual Rayleigh and Raman image intensities were normalized by the recorded laser pulse energy to account for shot-to-shot variations.

Since flows near the center of the gas heater outlet were temporally/spatially constant and each image was corrected for laser pulse energy and background, shot-to-shot variations accordingly were attributed to either signal noise or spurious interference sources. The major Rayleigh image interference source was Mie scattering from dust near the probe volume, while the major Raman spectral data interference was unwanted fluorescence from occasional optically induced breakdown of the hydrocarbon molecule. Dust particle Mie scattering was detected and masked from each Rayleigh image by a post-processing filter algorithm where intensity values at each pixel that were more than 3 normal standard deviations above the mean pixel value were removed. This process was repeated to ensure the computed mean and variance was minimally influenced by the outlier values. If more than 1% of the entire image was masked, the Raman/Rayleigh image pair was disregarded from the analysis. A similar fluorescence filter algorithm was applied to the Raman signal intensity.

Hydrocarbon Rayleigh cross-sections, σ_{HC}, normalized by the nitrogen Rayleigh cross-section were determined from the room temperature Rayleigh signal measurements. The interrogation region for the center 2 mm of the probe volume was spatially averaged to produce a signal intensity value, I_{Ray}, which was proportional to the ratio of the species weighted effective

Rayleigh cross-section and the mixture temperature. Accordingly the effective Rayleigh cross-sections for the heated gas mixtures had the form:

$$3.1 \qquad \sigma_{eff} = X_{N_2}\sigma_{N_2} + \left(1 - X_{N_2}\right)\sigma_{HC} = T\frac{I_{Ray}}{C_{Ray}} \;\Rightarrow\; \frac{\sigma_{HC}}{\sigma_{N_2}} = \frac{1}{1-X_{N_2}}\left(T\frac{I_{Ray}}{C_{Ray}} - X_{N_2}\right)$$

Here, C_{Ray} was the Rayleigh apparatus constant determined from the Rayleigh measurement of room-temperature nitrogen and equation 3.1 with σ_{eff} set to 1. Cross-sections for each hydrocarbon were then determined from the room temperature nitrogen diluted hydrocarbon gas flows and equation 3.1. Tabulated values are presented in Table 1 and compare favorably to calculated values based on experimental measured refractive indices [61].

Table 1. Computed Rayleigh cross-sections normalized by the N_2 cross-section for each hydrocarbon from the room temperature Rayleigh measurement.

Hydrocarbon	Normalized Rayleigh Cross-Sections (σ_{HC}/σ_{N2})
Methane (CH_4)	2.16
Acetylene (C_2H_2)	4.24
Ethylene (C_2H_4)	5.81
Ethane (C_2H_6)	6.54
Propane (C_3H_8)	12.90
Dimethyl Ether (CH_3OCH_3)	8.38

To determine the gas temperature for pure nitrogen flows, the thermocouple temperature at the quartz gas heater assembly exit was monitored while the variable transistor current was adjusted (see Figure 2). Although the quartz tube assembly was heavily insulated, an unknown amount of heat loss nonetheless occurred between the thermocouple measurement point and the laser probe volume just outside of the assembly outlet; the temperature was thus determined from the Rayleigh measurement. Once the temperature stabilized at a value, 100 Rayleigh images were recorded. The process was repeated in ~100 K increments until the maximum temperature of ~900 K was reached. Rayleigh images were processed as described above, with temperature determined from the integrated signal intensity and equation 3.1. From these measurements, a correlation was developed between the Rayleigh temperature and the thermocouple meter temperature indication, which was used to calibrate for the heated hydrocarbon/nitrogen mixtures. Note that no attempt was made to compensate for the differing mixture heat capacities, which led to small variations between the calibration and recorded Rayleigh temperature.

The recorded Raman signal, *k*, was the convolution of the unknown true signal distribution, ψ, and the apparatus transfer function, K. The transfer function corresponds to the monochromatic image of the laser beam profile on the Raman detector, and was obtained by scaling the Rayleigh scattering image of the laser beam by the measured magnification ratio for the Raman and Rayleigh systems. The signal as a function of ψ and the K was expressed as:

$$3.2 \qquad k(x) = \int \psi(\tau)\mathrm{K}(x|\tau)d\tau$$

Long term shot-to-shot beam profile variations led to varying spectral observations. To correct for this effect, the signal was separated using the Richardson-Lucy deconvolution [62, 63] routine where ψ was estimated from Bayesian inference. For this method, the conditional profile function K was interpreted as a continuous kernel K(x, τ) within the Fredholm integral equations and solved via Fourier methods. The reader is referred to references [62, 63] for more detailed description of the deconvolution approach. It should be noted that the solution to equation 3.2 was not unique and the estimated ψ values from each instantaneous image from the deconvolution routine could vary substantially. Furthermore, the measured transfer function was overly broad compared to the true spectral features, which prohibited a direct deconvolution to obtain accurate, resolved spectra. To get around this problem, the deconvolved spectra were subsequently convolved about a defined Gaussian profile, G(x, τ), that was a best fit to a representative profile K.

3.3 $$g(x) = \int \psi(\tau)\mathrm{G}(x,\tau)d\tau$$

Here, the Gaussian profile, G(τ), was defined as:

3.4 $$G(x) = \frac{1}{\omega\sqrt{2\pi}}\exp\left[-\frac{1}{2}\left(\frac{x-\mu}{\omega}\right)^2\right]$$

The profile width, $\omega = 4.0$, was centered at $x = 49$ in a 95 element vector. The reconstructed spectra gave a consistent observation value about which multiple spectra could be ensemble averaged together and opened the way for spectral decomposition methods described below. An additional advantage of expressing the measured spectra in terms of $g(x)$ was that this accounted for small but discernible spectral shifts that resulted from variations the beam profile position within the measurement region.

3.2 Spectral Decomposition

Large signal complexity for each hydrocarbon spectral signature, combined with the relative coarseness of the ~100 K temperature intervals at which the data was acquired meant that the data could not be directly interpolated for intermediate temperatures. Furthermore, the relatively low temperatures at which the heater data was collected (>900 K) meant that the spectra needed to be extrapolated up to more typical flame temperatures (~2000 K). A sensible way to determine the signal response was to decompose the recorded Raman spectra into basis functions and extrapolate these values to the desired temperature. The desired spectral response could then be reconstructed from these extrapolated values. For the present study, the basis functions were skew-normal density functions given as:

3.5 $$F = \sum_i A_i f_i$$

Here, F was the total modeled signal, f_i were the individual spectral components and A_i represented the corresponding peak amplitudes. The skew-normal distribution was a function of both the normal and cumulative distribution function (CDF) about a specified mean, with the CDF dependent variable multiplied by a skewness parameter, α:

3.6 $$f_i = 2G(\chi_i)\Phi(\alpha_i\chi_i)$$

Where the normal cumulative distribution function was defined as:

$$3.7 \qquad \Phi(\alpha_i x_i) = \int_{-\infty}^{x} G(\chi_i) d\chi = \frac{1}{2}\left[1 + \mathrm{erf}\sqrt{\alpha \frac{x_i - \mu_i}{2\omega_i}}\right]$$

Each basis function consisted of 4 dependent variables (A_i, α_i, μ_i, and ω_i), with the total number of basis functions determined by a Peak Finder routine that specified the peak location based on the signal differential. Dependent variable 'guess' values for each basis function were determined from best fit Gaussian profiles to the identified peak. Total peak number and overall peak spacing were controlled by a specified peak density and amplitude ratio. To determine if the peak location identified by the Peak Finder algorithm was sensible, a custom Matlab graphical user interface (GUI) was developed to visualize the projected peak location; a sample screen grab is given in Figure 4. Filenames and filter instructions were specified in an initialization file. Signal intensities were normalized by the Rayleigh temperature to correct for number density effects. The initial peak location was specified by a green 'x' in the main figure window.

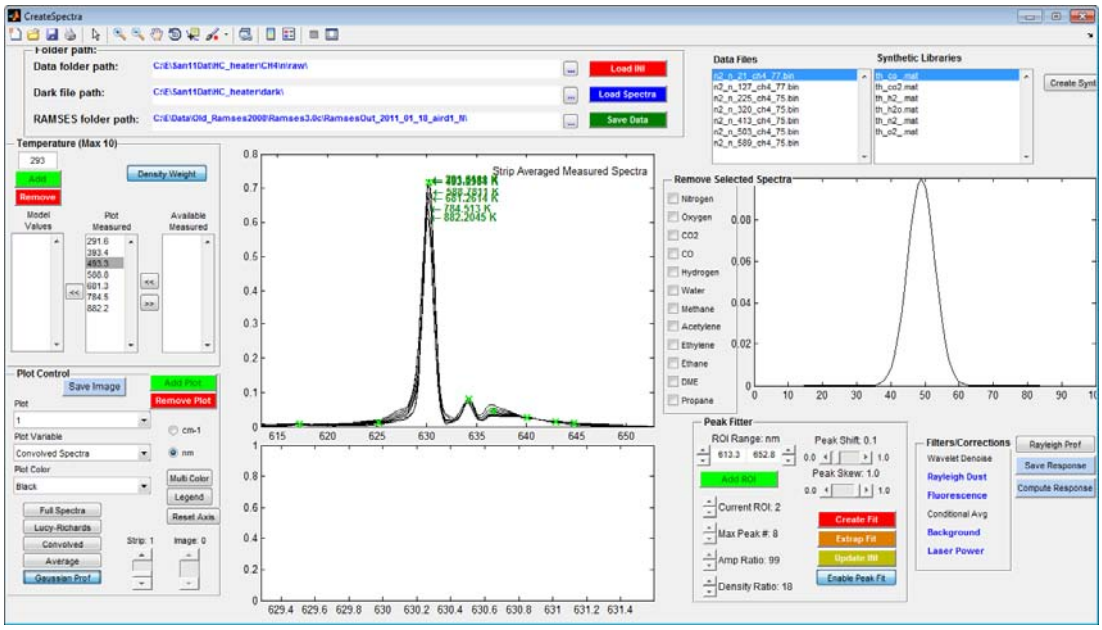

Figure 4. Screen grab of the Peak Finder routine from a custom GUI used to process recorded Raman spectra from the gas heater data.

Once suitable peak locations and initial dependent variables values were determined, a Peak Fit routine was used to optimize each dependent variable until the residual between the fit and reference signal was minimized. Large numbers of free parameters for each spectrum (40+) necessitated limits for the optimization routine. Amplitude and profile widths were bounded to ±50% of the initial value, while the peak skew and center deviation were limited by slider bars in the Peak Fitter GUI box.

3.3 Temperature Dependent Spectra

A linear fit was determined between each basis function dependent variable at each temperature and had the form:

$$A_i(T) = A_{0,i} + A_{1,i}T \quad (3.8)$$

$$\alpha_i(T) = \alpha_{0,i} + \alpha_{1,i}T \quad (3.9)$$

$$\mu_i(T) = \mu_{0,i} + \mu_{1,i}T \quad (3.10)$$

$$\omega_i(T) = \omega_{0,i} + \sigma_{1,i}T \quad (3.11)$$

Terms with subscripts 0 and 1 were constant coefficients with values given in Appendix A for each polarization and gas type. Although the linear fit allowed extrapolation of the spectral response to higher temperatures, extrapolated dependent variables could result in physically impossible values (i.e., negative amplitudes or peak widths). Accordingly, peaks with amplitudes less than zero or widths less than 0.25 were excluded. In Figure 5, a GUI screen grab of the reference spectra (black), fit spectra output by Peak Fit (red), and modeled spectra produced from equations 3.5-3.11 (blue) is shown for methane. The ratio of the dilution corrected integrated portion of the nitrogen spectrum was recorded at each temperature and scaled to match the calculated nitrogen spectral libraries from RAMSES. This scaling factor was then applied to the dilution corrected hydrocarbon portion of the spectra. To generate model spectra from an arbitrary transfer function, the calculated empirical spectra must be deconvolved by the reference Gaussian and then convolved with the measured transfer function. A more comprehensive discussion of signal post-processing and fit quality is discussed in the Section 4.

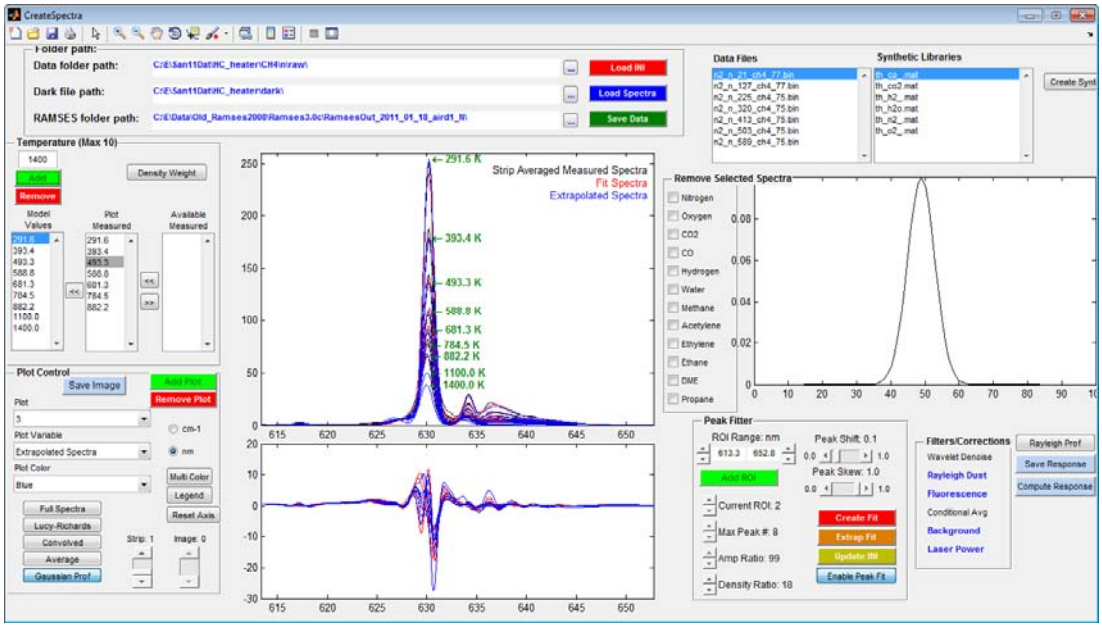

Figure 5. Signal processing GUI screen grab of the reference (black), fit (red) and modeled spectra (blue) for the C-H stretch region of the unfiltered methane signal.

3.4 Laminar Vertical Flame Post-Processing

The vertical laminar flame was physically positioned such that the flame front was centered along the 6 mm probe volume length. Raman spectra were acquired using the full spectral resolution of the camera (~0.12 nm/pixel) with 100 µm hardware binning in the spatial direction (10 pixels) along the 6 mm probe volume for 60 strips of overall data. For the Rayleigh images, the camera resolution was 340×90 pixels. Simultaneous Raman and Rayleigh imaging for the

methane and dimethyl ether flames described in Section 2 was performed in 500 image increments 10 times throughout the test day for a total of 5,000 Raman/Rayleigh image pairs. Like the heater data, the Raman imaging was performed under the 3 polarization conditions. Reference background image sequences were acquired at multiple times throughout to correct for potential background drift. The background correction was similar to the correction of the heated gas data. Sequences of 100 room temperature 'air' images, where the laser system was active but there was no gas flow into the probe volume, were also acquired to provide a benchmark response of the oxygen and nitrogen Raman scattering spectra.

The methane and DME vertical laminar flames had minimal flow strain and were nearly planar, which justified *a priori* determination of species concentrations along flame front by CHEMKIN PRO [64] for unstrained 1D premixed flames with multi-component transport and the Soret effect included. Flame chemistry was handled by two well-validated kinetics mechanisms: the GRI Mech 3.0 mechanism [65] for methane, and the Zhao et al. mechanism [66] for DME. Simulation results for species mole fraction as a function of temperature are presented in Figure 6 for both the methane and DME 1D flames. The upper graph displays the relative concentrations for the major constituents, while the lower graphs display the mole fractions of the parent fuel relative to the principal hydrocarbon intermediates. From these graphs, it can be observed that intermediate hydrocarbon concentrations were negligible for methane flames, even at elevated temperatures where the methane consumption rates were greatest. However, for the DME flames there were non-negligible concentrations that appeared at temperatures as low as 600 K. Note that formaldehyde (CH_2O) had the highest intermediate hydrocarbon concentrations for the DME flame, but experimentally obtaining spectra from these molecules through the use of the gas heater assembly was beyond the current capabilities. This was due to the complexities required to generate known steady flow rates of gas-phase formaldehyde without the presence of more complex aldehydes in the flow stream. Thus, formaldehyde contributions were evaluated from the laminar flame data with the spectral contributions from the other constituents subtracted off. Further discussion is given in Section 4.

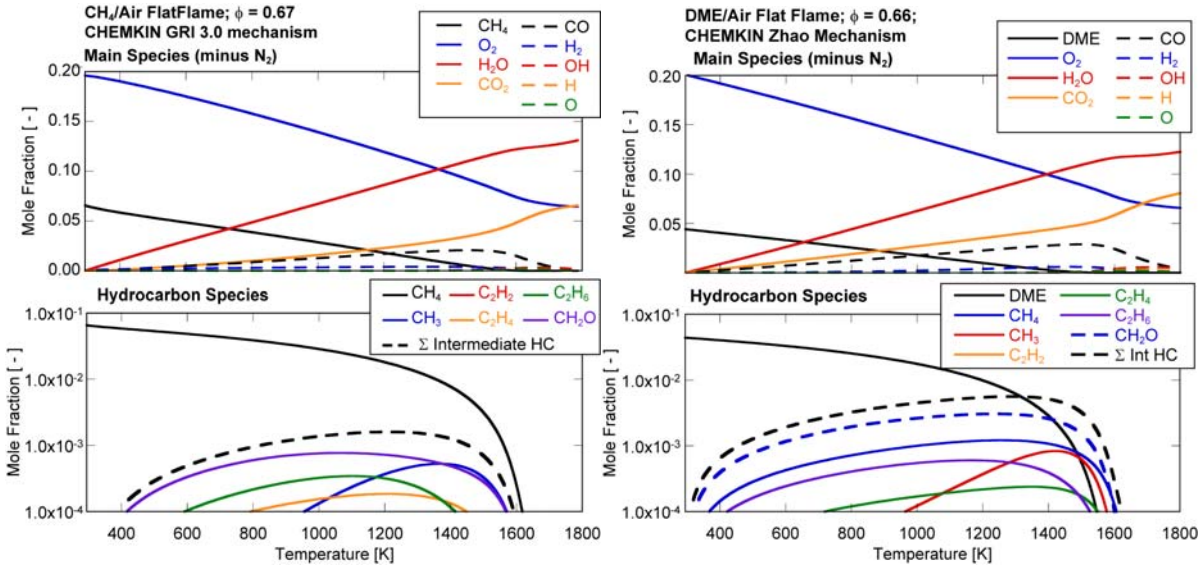

Figure 6. Laminar flame species concentrations as a function of temperature from CHEMKIN PRO 1D calculations for lean methane and dimethyl-ether fueled flames.

Finally, to account for the unstable flame front position within the interrogation probe volume, a conditional flame position algorithm was developed. The routine evaluated the flame front position from each recorded sample based on the corresponding Rayleigh measurement at each strip. For this routine, the measured effective Rayleigh cross-section was computed from equation 3.1. This value was then correlated to the computed effective Rayleigh cross-section from equation 1.2 with the mixture composition obtained from the CHEMKIN PRO simulation results and the species specific Rayleigh cross-sections obtained from either Table 1 for the hydrocarbons or Gardiner et al. [61] for all other species. Spectra from each of the 5,000 images each with 20 strips of data (for a total of up to 100,000 samples overall) were grouped into 20 K temperature bins and conditionally averaged together. To account for the non-uniform beam profiles that resulted shifts of spectral data, the signal was deconvolved by the corresponding single-shot apparatus transfer function and then convolved with the reference Gaussian transfer function as described in Section 3.1. For each 20 K bin, the number of valid samples ranged from several dozen to several hundred depending on the relative width in the flame front for the given bin.

4. RESULTS

The development of empirical spectral libraries from the heated gas and laminar flame data, obtained and processed as described in Sections 2 and 3, is presented in this section. In Section 4.1 the conversion of post-processed Raman spectra into empirical libraries is outlined. Due to the large number of examined conditions, only an example condition (unfiltered DME) is considered, with additional libraries included in Appendix A. In Section 4.2, results from the laminar flame data are presented, along with a qualitative comparison of model generated spectra relative to measured values. Note that the absence of a model formaldehyde spectrum prevented a truly quantitative comparison. However, the subtraction of the model spectrum from the measured value allowed an approximate measurement of the formaldehyde Raman spectra.

4.1 Heated Gas Mixtures

The project goal was to generate hydrocarbon spectral libraries that covered a broad range of flame temperatures using the Raman/Rayleigh data collected from the gas heater experiments. An example of the process used to deconstruct post-processed recorded spectra into basis functions and then extrapolate these basis values to higher temperatures to generate spectral libraries is discussed here. Recorded spectra from an unfiltered DME Raman spectrum at room temperature and processed as described in Section 3.1 but prior to the deconvolution is presented in Figure 7 for the C–C and C–H regions.

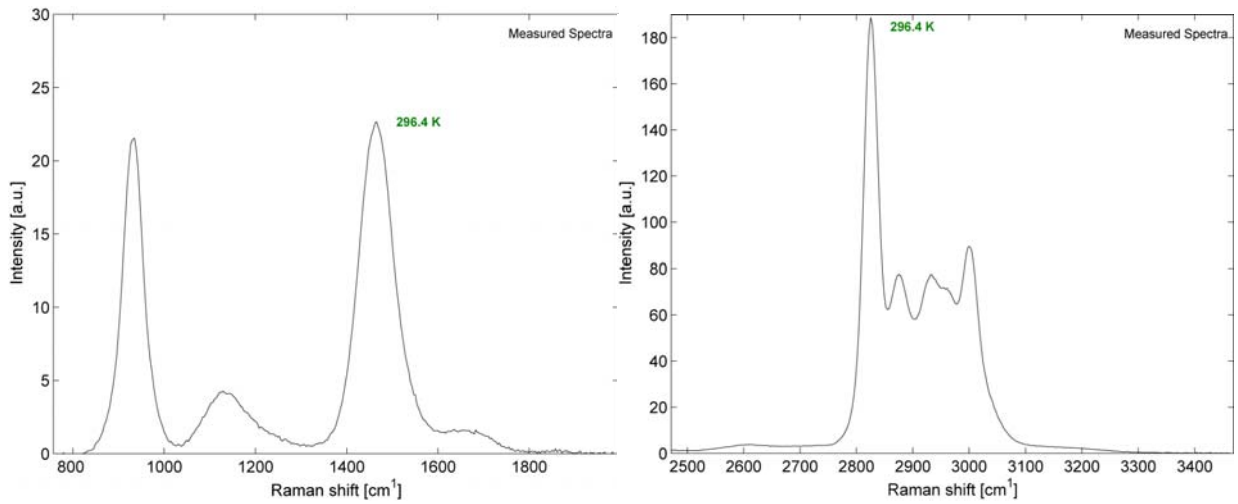

Figure 7. Post-processed unfiltered Raman spectral measurements of DME (CH_3OCH_3) before deconvolution for the C–C (left) and C–H (right) stretch regions.

The measured spectrum in Figure 7 was deconvolved via the Richardson-Lucy deconvolution described in Section 3.1 and then convolved with the reference Gaussian function described in the same section. Both the deconvolved and convolved spectra are presented alongside the measured spectrum in Figure 8 along with the residuum between the measured and convolved spectra. At all regions the deviation of the convolved spectra from the reference spectrum was small (<10%) and was principally due to slight shifts of the sharp peaks, which amplified the errors that resulted from the change in transfer function. Similar data processing was performed for the spectra from each temperature.

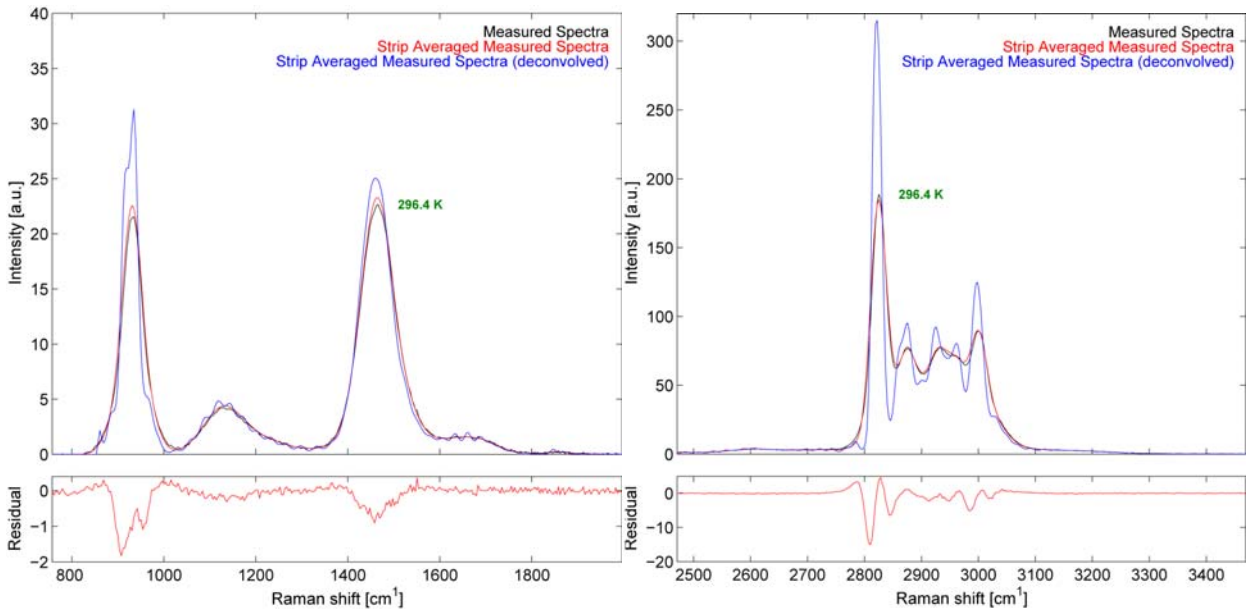

Figure 8. Unfiltered Raman spectral measurements of DME (CH_3OCH_3) before the deconvolution (black), once devonvolved (blue), and after being convovled with the reference Gaussian transfer function (red) for the C–C (left) and C–H (right) regions.

Basis function dependent variables were determined from the Peak Fit routine described in Section 3.2 for the measured spectra at each temperature, and have been plotted in Figure 9. These values are compared to model values determined from the extrapolated algorithm in Section 3.3; the agreement was very good for all variables throughout the temperature range.

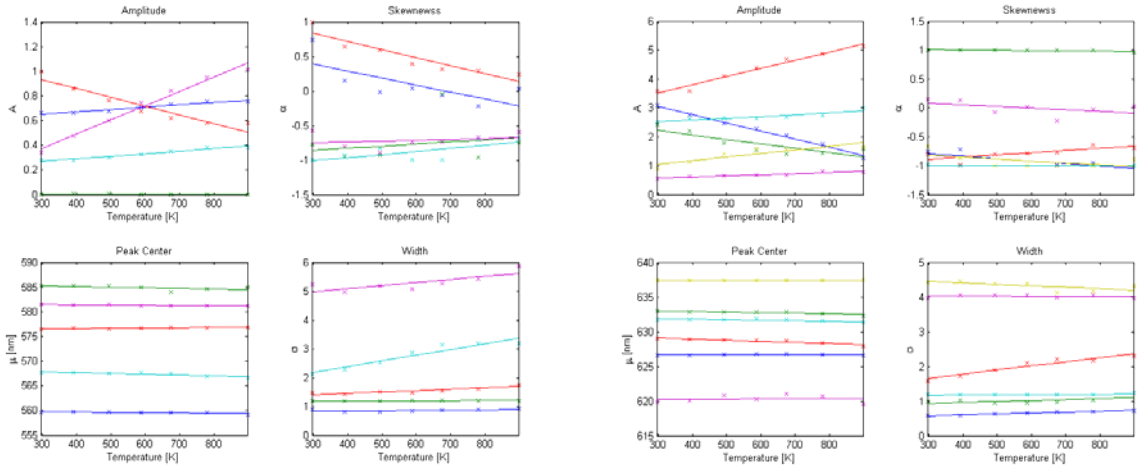

Figure 9. Comparison of fit (symbols) to modeled (solid lines) basis function dependent variable coefficients (equations 3.8 - 3.11) from the C–C (left) and C–H (right) region the unfiltered DME (CH_3OCH_3) Raman spectrum.

From the modeled basis values and equations 3.5–3.7, extrapolated spectra were generated at the reference measurement temperatures and are presented in Figure 10 alongside the reference

and fit spectra for both the C–C and C–H regions. Calculated fit and modeled spectra residuum relative to the reference spectra are also displayed and were roughly comparable, which suggests that the linear extrapolation technique was able to sufficiently capture both the spectral characteristics across the calibration range. Two additional spectra were generated from the extrapolated basis values at temperatures beyond the calibration range (1100 and 1400 K) and were likewise plotted in Figure 10. Although there were no measurement data to compare against, the qualitative trends in the evolution of the characteristics seem to be suitable captured. Improved performance testing will come from comparisons to the laminar vertical flame data in Section 4.2.

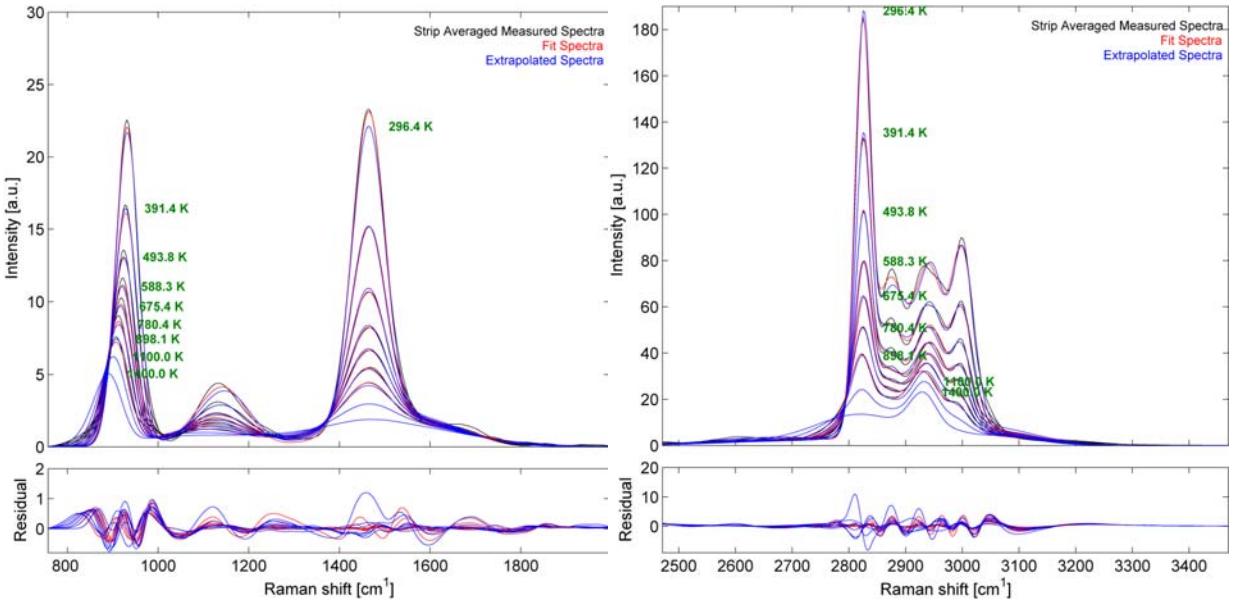

Figure 10. Reference (black), fit (red), and model (blue) spectra for the unfiltered DME (CH_3OCH_3) Raman spectral data.

Since the hybrid data reduction method involves on-chip integration of defined spectral bounds, the absolute position, shape, and magnitude of the spectral features are less important than the integrated response between these defined bounds. In Table 2, the original integration bounds used to process methane and hydrogen flames in the multiscalar measurement facility [35, 36, 38, 60] along with updated integration regions that account for the additional hydrocarbon species are tabulated. The locations of the updated integration bounds, although somewhat arbitrary, were selected by visual inspection to isolate dominant spectral features from each on the major hydrocarbon intermediates.

Table 2. Original and updated Raman spectral shift integration regions.

Channel	Original Integration Region [cm^{-1}]		Updated Integration Region [cm^{-1}]	
	Start	**End**	**Start**	**End**
F560	761	1096	761	1118
CO_2–a	1129	1333	1129	1260
CO_2–b	1336	1483	1263	1405
CO_2–c	–	–	1408	1483
O_2–a	1487	1589	1487	1589
O_2–b	–	–	1593	1659
BG_1	1738	1946	1711	1844
C_2H_2	–	–	1882	2012
CO	2016	2197	2016	2197
N_2	2200	2421	2200	2421
HC–a	2798	2914	2769	2890
HC–b	2917	2972	2893	2937
HC–c	2975	3262	2940	2990
HC–d	–	–	2993	3234
H_2O	3429	3712	3429	3712
BG_2	3781	3895	–	–
H_2	3963	4227	3963	4227
BG_3	4294	4500	4294	4500

Measured and extrapolated integrated response values based on the updated integration bounds identified in Table 2 for the C–C and C–H regions are plotted on a semi-log scale against temperature in Figure 11. The agreement between the measured and extrapolated integrated response was excellent.

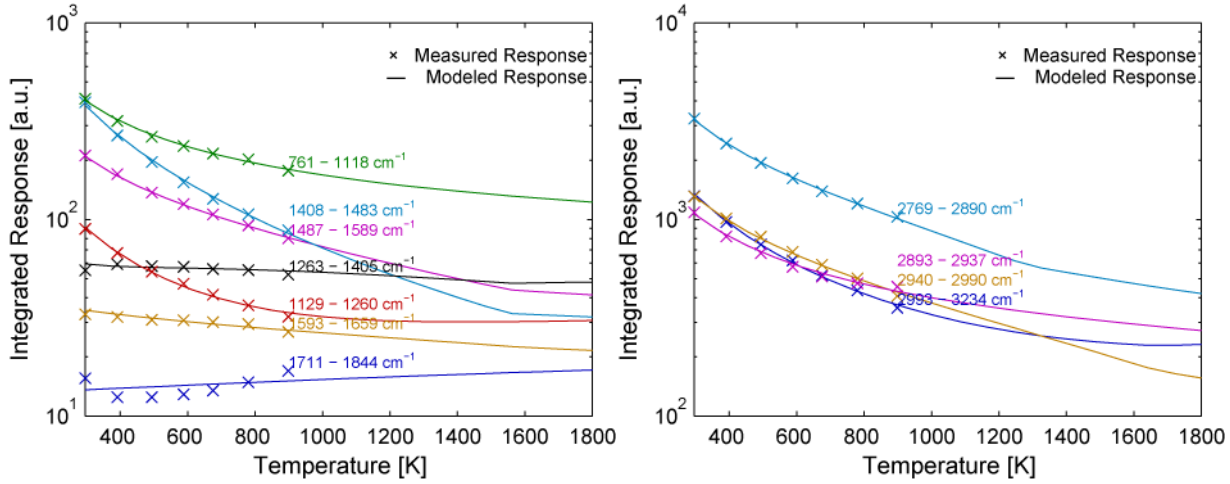

Figure 11. Updated Raman spectral shift integration response unfiltered DME (CH_3OCH_3) for the C–C (left) and C–H (right) rovibrational regions.

The extrapolated integrated response values exhibit qualitatively consistent trends for temperatures beyond the calibration range. Some integration regions had discontinuous changes in the integrated response (e.g., CO_2–c, O_2–a, and HC–a) as certain peaks were removed once

extrapolated amplitudes or widths for fell below the threshold values established in Section 3.3. These results highlight the need for a smoothing mechanism to more gradually phase out the impact of the spurious peaks. Nonetheless, the overall discontinuities were small and the absolute integrated response values at the discontinuity points were relatively low; thus it was expected there would be negligible impact on the species determination from the hybrid method.

4.2 Laminar Vertical Flames

Vertical laminar flames for both methane and dimethyl-ether were processed as described in Section 3.4, with all spectra convolved to the uniform reference Gaussian transfer function. Sample methane and DME vertical laminar flame spectra from select temperatures determined from the Rayleigh signal and equation 3.1 are displayed in Figure 12. Spectral contributions from CO_2, O_2, CO, N_2, and H_2O along with the C–C and C–H hydrocarbon rovibrational stretch regions are identified.

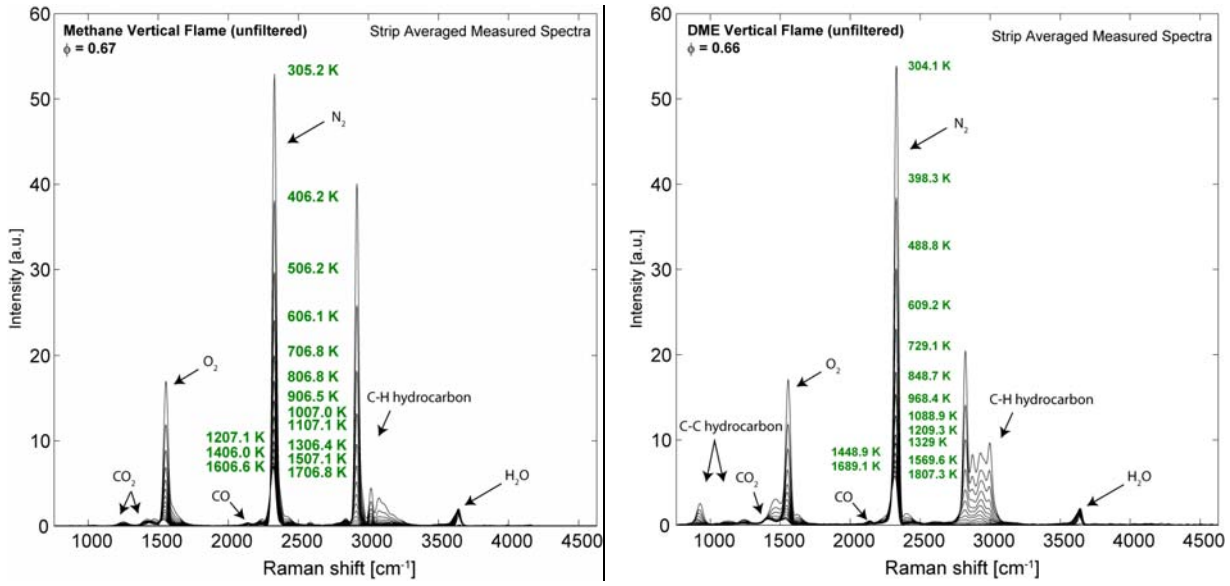

Figure 12. Reference unfiltered Raman spectra from laminar vertical methane (left) and DME (right) flames over a broad temperature range.

To model the methane flame spectra, species mole fractions were acquired from 1D flame calculations for the given temperature. Calculated RAMSES libraries convolved with the reference Gaussian transfer function were used to account for the reactants, products, and major intermediates (CO_2, O_2, CO, N_2, H_2, and H_2). Methane spectra were modeled using equations 3.5–3.11 and the coefficient values given in Appendix A. Model spectra are plotted in Figure 13 (in red) relative to the reference spectra from Figure 12 along with the residuum between the two. Although the residuum in the C–H rovibrational region was somewhat larger than anywhere else in the spectrum, the difference was still within ±10% of the measured value and was primarily due to slight spectral peak location shifts.

Also plotted in Figure 13 is the integrated response from the updated bin regions identified in Table 2 with intensity counts greater than 10. Agreement for non-hydrocarbon channel measured (symbols) and modeled (solid lines) integrated response values was excellent, which suggests

that the mixture compositions determined from the 1D laminar flame calculations and the calculated spectral libraries produces from RAMSES performed well. Furthermore, along the primary methane spectrum hydrocarbon channel (HC-b: 2893 – 2937 cm^{-1}), the agreement was likewise very good throughout the entire temperature range. Agreement between the secondary hydrocarbon channels, however, was not as clean. Model spectra integrated response was underpredicted above ~900 K for HC-a (2769 – 2890 cm^{-1}), above ~800 K for channel HC-d (2993 – 3234 cm^{-1}), and for HC-c (2940 – 2990 cm^{-1}) throughout the entire temperature range. The model spectra integrated response was also overpredicted for HC-a (2769 – 2890 cm^{-1}) for temperatures below ~900 K. It should be noted that contributions from the unknown formaldehyde and methyl radical (CH_3) spectra were not included and may have accounted for some of the observed deviations from the measurement.

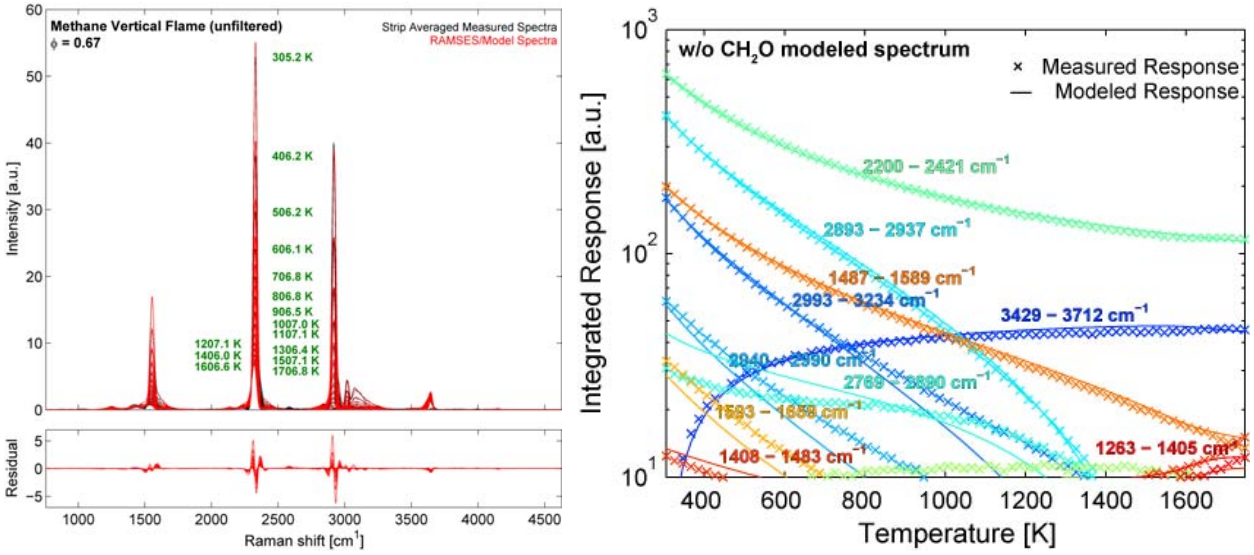

Figure 13. Laminar reference (black) and modeled (red) Raman spectra for the unfiltered methane flame along with a comparison of the measured and modeled integrated response.

Similar model spectra were generated for the DME vertical laminar flame except that contribution of hydrocarbon intermediates, minus the unknown formaldehyde and methyl radical spectra, were included. These model spectra are compared to the reference spectra in the hydrocarbon C–H rovibrational stretch region at moderate flame temperatures (600 – 1400 K) in the leftmost plot of Figure 14. While the agreement between the measured and modeled values was very good in most regions, the model spectra consistently underpredicted the spectral response in a region centered at a Raman spectral shift of around 2800 cm^{-1}. The offset was likely due of the absence of a formaldehyde spectrum as this region corresponded almost exactly to the Raman shift of the dominant spectral peak observed for gas phase room temperature formaldehyde (2780 cm^{-1}) by Chapput et al. [67] and expected formaldehyde mole fractions at these temperatures were non-negligible relative to parent fuel concentrations. The relatively large magnitude of the residuum in this region suggests a rough formaldehyde spectrum can be generated from this region.

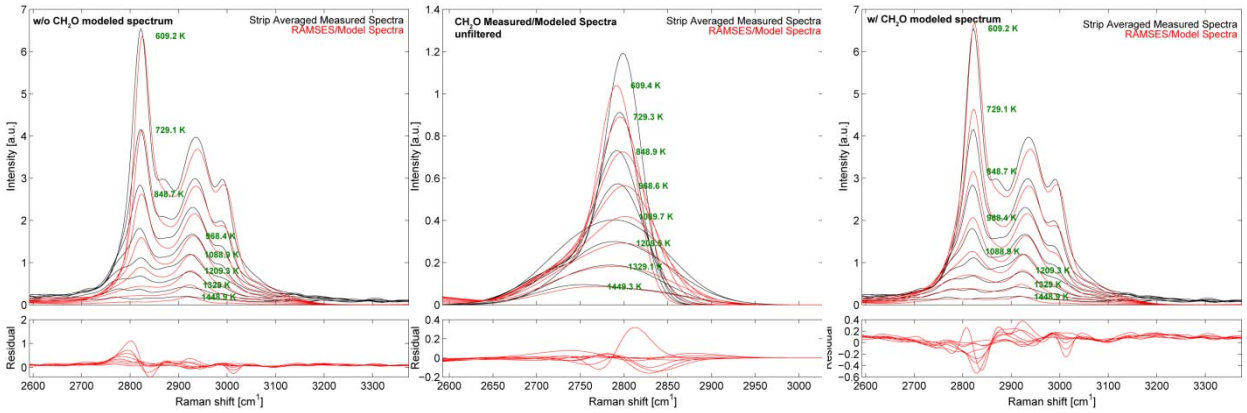

Figure 14. Reference (black) and modeled (red) Raman spectra for the unfiltered DME laminar vertical flame along the C–H rovibrational stretch region without a model formaldehyde spectrum (left), a formaldehyde spectrum generated from the signal residuum (center), and updated spectra that includes the new formaldehyde spectra (right).

To generate the model formaldehyde spectrum, the Peak Finder/Fit routines described in Sections 3.2 and 3.3 were applied to the reference spectrum with empirical spectra from DME and the hydrocarbon intermediates at concentrations predicted by the 1D laminar flame calculations subtracted off. Although expected formaldehyde mole fractions were relatively small (~0.003) and the overlap between the DME and intermediate hydrocarbon spectra was strong, there nonetheless appeared to be sufficient resolution to obtain coarse formaldehyde spectra. Modeled spectra were produced from using the methods described in Sections 3.2 and 3.3, with model coefficients tabulated in Appendix A. The agreement between the empirical and reference corrected spectra was fairly good when the low signal intensities are considered. The rightmost plot in Figure 14 is of the revised model spectra with the addition of the model formaldehyde spectrum and plotted against the original reference spectra. The agreement between the reference and modeled spectra improved substantially.

Integrated spectra for the laminar vertical DME flame, both with and without the contribution of the formaldehyde spectra, are plotted in Figure 15. Note that the modeled integrated response along the H_2O channel was significantly underpredicted at temperatures below ~900 K, which suggests the performance of the Zhao kinetics mechanism [66] did not perform as well as the GRI mechanism [65]. Nonetheless, the agreement along the other non-hydrocarbon channels was good. The principal hydrocarbon channel for the DME spectra was HC-a (2769 – 2890 cm^{-1}), which also overlapped the expected formaldehyde spectra. Without the impact of model formaldehyde spectra included, model integrated spectra underpredicted the measured values at moderate flame temperatures (~500 – 1300 K). But once the formaldehyde spectra was included, the model and measured integrated response along this channel matched almost exactly. The agreement along the secondary hydrocarbon channels was likewise very good. It should be cautioned, however, that since the formaldehyde spectra were constructed from the residuum of the measured reference spectra with modeled hydrocarbon spectral contributions subtracted off, errors in the modeled DME and intermediate hydrocarbon spectra may have propagated into the modeled formaldehyde spectra. Accordingly, a priority for follow-on research should be to obtain quantitative gas-phase formaldehyde Raman spectra at controlled concentrations and at

relevant intermediate flame temperatures as was done for the current study for select hydrocarbon species.

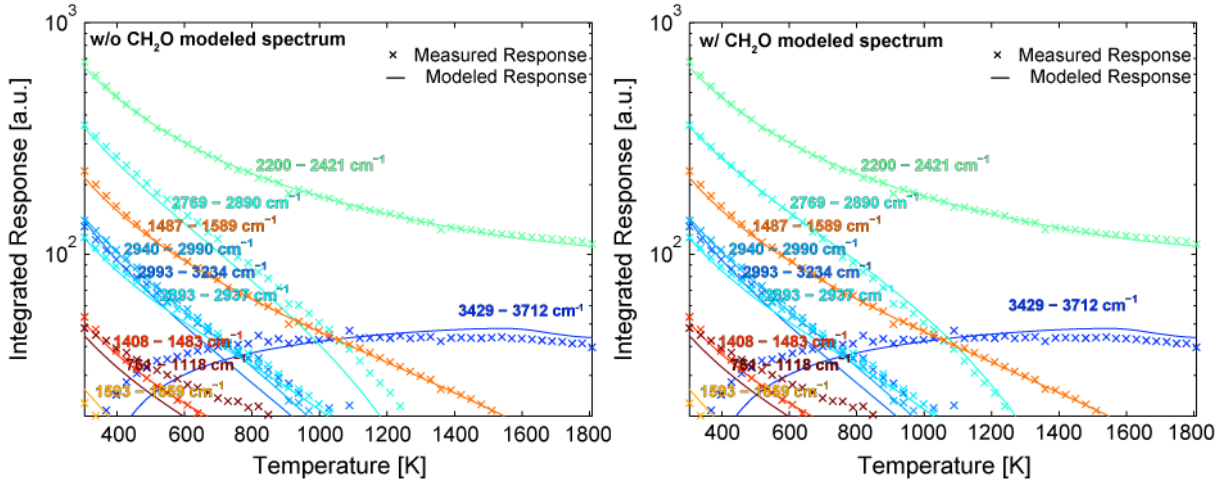

Figure 15. Measured (symbols) and modeled (solid line) integrated Raman spectral response for the unfiltered DME vertical flame without (left) and with (right) the model formaldehyde spectra.

Finally, it should be noted that similar processing of the s-polarized spectra was performed and with model formaldehyde spectra obtained using the methods described above; basis function model coefficients were also tabulated in Appendix A. Due to the weak signal intensity for the p-polarization condition, reference model formaldehyde spectra could not be obtained. Instead these spectra can be produced from the difference between the unfiltered model and s-polarized model spectra.

5. SUMMARY AND CONCLUSIONS

To improve the applicability of spontaneous Raman spectroscopy as a combustion diagnostic for fuel types more complex than methane, empirical spectral libraries were generated for dominant hydrocarbon intermediates. The multiscalar measurement facility located at Sandia/CA was used to record the Raman spectra of select nitrogen diluted hydrocarbon samples (C_2H_2, C_2H_4, C_2H_6, C_3H_8, CH_4, and DME), which were heated to temperatures up to 900 K using a a custom quartz tube heater assembly. Recorded spectra were post-processed to correct for background/laser power fluctuations, remove spurious interferences sources, and then convolved with a common (Gaussian) transfer function so that the single-shot images could be averaged across the 100-shot ensemble. Corrected and averaged spectra from each temperature, determined from a corresponding Rayleigh profile measurement and known Rayleigh cross-section values, were then decomposed into basis functions by a custom Peak Fit routine. The linear dependence of the basis values on temperature enabled extrapolation of the basis values to higher temperatures; coefficients for the linear extrapolation are tabulated in Appendix A for all hydrocarbons. Empirically modeled spectra were generated for three polarization conditions: unfiltered, s-polarized, and p-polarized, so that the spectra would be applicable to polarization separation techniques that are used to remove stray soot incandescence and fluorescence from the recorded Raman signal. This also allows for measurements that include only the s-polarized scattering signal, which is a more common strategy to reduce the relative contribution of flame luminosity and fluorescence interference.

Performance testing of the developed spectral libraries was accomplished using data measured from lean methane and DME vertical laminar flames. Species composition for each flame was determined from 1D laminar flame simulations using well-validated kinetics mechanisms. An effective Rayleigh signal was produced from the expected compositions and correlated to the measured Rayleigh intensity from the flame. A custom conditional averaging routine was developed that binned Raman spectral information into 20 K bins and ensemble averaged together to improve SNR. To model the flame spectra, species composition values from the 1D flame calculations were again used. Spectra from non-hydrocarbon reactants, products, and major intermediates (CO_2, H_2O, N_2, O_2, CO, and H_2) were modeled using calculated spectral libraries (RAMSES), while hydrocarbon spectra were modeled from the empirically generated spectral libraries developed in the present study. Very good agreement was observed between the modeled and measured Raman spectra from the methane laminar vertical flame at all temperatures range for both the hydrocarbon and non-hydrocarbon spectra. The agreement along the C–H rovibrational stretch region for the DME laminar vertical flame, corrected for hydrocarbon intermediates, was not as good. The difference was attributed to the absence of formaldehyde model spectra since the peak locations were consistent with a published room temperature spectrum. Model formaldehyde spectra were generated from the measured spectra minus the model DME and hydrocarbon intermediate spectra. Once the model formaldehyde was included, the agreement across the entire C–H stretch region was found to be excellent.

The diagnostic development allows for temporally and spatially resolved flame measurements of speciated hydrocarbon concentrations whose parent is more chemically complex than methane – critical data needed to validate increasingly complex flame simulations. Additional work is needed, however, to improve the resolution and accuracy of the model formaldehyde spectrum.

6. REFERENCES

1. J. E. Dec, C. Espey, *SAE Transactions*, **104**, (1995).
2. R. W. Schefer, *Int J Hydrogen Energy*, **28**, 1131, (2003).
3. J. C. Oefelein, V. Yang, *J Propul Power*, **14**, 843, (1998).
4. International Workshop on Measurement and Computation of Turbulent Nonpremixed Flames (TNF), <http://www.ca.sandia.gov/TNF>.
5. S. B. Pope, *Prog Energ Combust*, **11**, 119, (1985).
6. S. B. Pope, *Computational Fluid Dynamics Symposium on Aeropropulsion*, **3078**, 335, (1991).
7. S. Candel, D. Veynante, F. Lacas, N. Darabiha, C. Rolon, *Combust Sci Technol*, **98**, 245, (1994).
8. P. A. Libby, F. A. Williams, *Turbulent Reacting Flows*, Academinc Press, New York, (1994).
9. D. C. Haworth, *Prog Energ Combust*, **36**, 168, (2010).
10. S. Navarro-Martinez, A. Kronenburg, F. Di Mare, *Flow Turbul Combust*, **75**, 245, (2005).
11. A. W. Vreman, B. A. Albrecht, J. A. van Oijen, L. P. H. de Goey, R. J. M. Bastiaans, *Combust Flame*, **153**, 394, (2008).
12. V. Sankaran, T. G. Drozda, J. C. Oefelein, *P Combust Inst*, **32**, 1571, (2009).
13. J. Floyd, A. M. Kempf, A. Kronenburg, R. H. Ram, *Combust Theor Model*, **13**, 559, (2009).
14. A. Mardani, S. Tabejamaat, M. Ghamari, *Combust Theor Model*, **14**, 747, (2010).
15. R. W. Dibble, A. R. Masri, R. W. Bilger, *Combust Flame*, **67**, 189, (1987).
16. S. H. Starner, R. W. Bilger, R. W. Dibble, R. S. Barlow, *Combust Flame*, **83**, 63, (1991).
17. A. R. Masri, R. W. Dibble, R. S. Barlow, *Combust Flame*, **91**, 285, (1992).
18. D. G. Pfuderer, A. A. Neuber, G. Fruchtel, E. P. Hassel, J. Janicka, *Combust Flame*, **106**, 301, (1996).
19. A. Brockhinke, A. T. Hartlieb, K. Kohse-Hoinghaus, D. R. Crosley, *Appl Phys B-Lasers O*, **67**, 659, (1998).
20. F. Rabenstein, A. Leipertz, *Appl Optics*, **37**, 4937, (1998).
21. M. M. Tacke *et al.*, *Twenty-Seventh Symposium (International) on Combustion, Vols 1 and 2*, 1139, (1998).
22. R. S. Barlow, J. H. Frank, *Twenty-Seventh Symposium (International) on Combustion, Vols 1 and 2*, 1087, (1998).
23. P. A. Nooren, M. Versluis, T. H. van der Meer, R. S. Barlow, J. H. Frank, *Appl Phys B-Lasers O*, **71**, 95, (2000).
24. W. Meier, O. Keck, *Meas Sci Technol*, **13**, 741, (2002).
25. R. S. Barlow, A. N. Karpetis, J. H. Frank, J. Y. Chen, *Combust Flame*, **127**, 2102, (2001).
26. A. N. Karpetis, R. S. Barlow, *P Combust Inst*, **29**, 1929, (2002).
27. C. Schneider, A. Dreizler, J. Janicka, E. P. Hassel, *Combust Flame*, **135**, 185, (2003).
28. R. S. Barlow, A. N. Karpetis, *Flow Turbul Combust*, **72**, 427, (2004).
29. C. Dreyer, T. Parker, M. A. Linne, *Appl Phys B-Lasers O*, **79**, 121, (2004).
30. J. Egermann, T. Seeger, A. Leipertz, *Appl Optics*, **43**, 5564, (2004).
31. R. S. Barlow, J. H. Frank, A. N. Karpetis, J. Y. Chen, *Combust Flame*, **143**, 433, (2005).
32. S. P. Kearney, R. W. Schefer, S. J. Beresh, T. W. Grasser, *Appl Optics*, **44**, 1548, (2005).
33. A. N. Karpetis, R. S. Barlow, *P Combust Inst*, **30**, 665, (2005).
34. R. S. Barlow, *P Combust Inst*, **31**, 49, (2007).

35. R. S. Barlow, H. C. Ozarovsky, A. N. Karpetis, R. P. Lindstedt, *Combust Flame*, **156**, 2117, (2009).
36. R. S. Barlow, G. H. Wang, P. Anselmo, M. S. Sweeney, S. Hochgreb, *P Combust Inst*, **32**, 945, (2009).
37. U. Aaronson *et al.*, paper presented at the SAE World Congress, 2009-01-1357, Detroit, MI, April 20-23, 2009.
38. F. Fuest, R. S. Barlow, J. Y. Chen, A. Dreizler, *Combust Flame*, **159**, 2533, (2012).
39. S. Lederman, *Prog Energ Combust*, **3**, 1, (1977).
40. M. H. Hayes, *Statistical Digital Signal Processing and Modeling*, Wiley, (1996), pp. 624.
41. P. C. Miles, *Appl Optics*, **38**, 1714, (1999).
42. M. Knapp *et al.*, *Appl Optics*, **35**, 4009, (1996).
43. R. S. Barlow, C. D. Campbell, R. W. Pitz, in *Applied Combustion Diagnostics*, Edited by: K. Kohse-Héinghaus, J. B. Jeffries, CRC Press, New York, (2002).
44. D. Geyer, *1D-Raman/Releigh Experiments in a Turbulent Opposed Jet*. PhD Thesis, Technical University of Darmstadt (2005).
45. D. A. Stephenson, *J Quant Spectrosc Ra*, **14**, 1291, (1974).
46. H. Tennekes, J. L. Lumley, *A First Course in Turbulence*, The MIT Press, Cambridge, MA, (1972).
47. S. B. Pope, *Turbulent Flows*, Cambridge University Press, Cambridge, UK, (2000).
48. D. C. Wilcox, *Turbulence Modeling for CFD*, D C W Industries, La Cañada, CA, ed. 3, (2006).
49. F. A. Williams, *Combustion Theory*, Perseus Books, Reading, MA, ed. 2, (1985).
50. R. W. Bilger, S. H. Starner, R. J. Kee, *Combust Flame*, **80**, 135, (1990).
51. P. Givi, *Prog Energ Combust*, **15**, 1, (1989).
52. S. B. Pope, Computations of Turbulent Combustion: Progress and Challenges. *P Combust Inst*, **23,** 591, 1990.
53. F. Gao, E. E. Obrien, *Phys Fluids a-Fluid*, **5**, 1282, (1993).
54. P. J. Colucci, F. A. Jaberi, P. Givi, S. B. Pope, *Phys Fluids*, **10**, 499, (1998).
55. J. C. Oefelein, *Prog Aerosp Sci*, **42**, 2, (2006).
56. H. Pitsch, *Annu Rev Fluid Mech*, **38**, 453, (2006).
57. E. Knudsen, S. H. Kim, H. Pitsch, *Phys Fluids*, **22**, (2010).
58. P. Givi, *Aiaa J*, **44**, 16, (2006).
59. T. G. Drozda, M. R. H. Sheikhi, C. K. Madnia, P. Givi, *Flow Turbul Combust*, **78**, 35, (2007).
60. F. Fuest, R. S. Barlow, D. Geyer, F. Seffrin, A. Dreizler, *P Combust Inst*, **33**, 815, (2011).
61. W. C. Gardiner, Y. Hidaka, T. Tanzawa, *Combust Flame*, **40**, 213, (1981).
62. L. B. Lucy, *Astron J*, **79**, 745, (1974).
63. W. H. Richards, *J Opt Soc Am*, **62**, 55, (1972).
64. CHEMKIN-PRO, Release 15112, Reaction Design, San Diego, CA, (2011).
65. G. P. Smith *et al.*, GRI-Mech 3.0, <http://www.me.berkeley.edu/gri_mech>.
66. Z. Zhao, M. Chaos, A. Kazakov, F. L. Dryer, *Int J Chem Kinet*, **40**, 1, (2008).
67. A. Chapput, B. Roussel, G. Fleury, *J Raman Spectrosc*, **1**, 507, (1973).

APPENDIX A: EMPIRCAL HYDROCARBON SPECTRAL LIBRARIES

Complete empirical spectral libraries for all 6 hydrocarbons examined (C_2H_2, C_2H_4, C_2H_6, C_3H_8, CH_4, and DME) are summarized here for both the C–C and C–H rovibrational stretch regions. Model coefficients for the basis function from equations 3.8 - 3.11 are included in tables at the three polarization conditions (unfiltered, s-polarized, and p-polarized). It should be noted that the model coefficients are only valid for spectra in nanometer wavelength space. Comparisons of the measured, fit, and modeled spectra, along with the modeled and measured integrated spectral response are included in separate figures below the tables.

Table 3. Basis function dependent variable coefficients within the unfiltered C–C rovibrational stretch region (~500 – 2000 cm^{-1} Raman shift) for all hydrocarbons.

$A_{0,i}$	$A_{1,i}$	$\alpha_{0,i}$	$\alpha_{1,i}$	$\mu_{0,i}$	$\mu_{1,i}$	$\omega_{0,i}$	$\omega_{1,i}$
			C_2H_2				
4.010E+00	-1.336E-03	-8.378E-01	-2.680E-04	5.951E+02	-1.790E-04	5.849E-01	2.080E-04
3.918E-01	3.900E-04	3.714E-01	9.290E-04	5.940E+02	-1.069E-03	3.298E+00	-3.198E-03
			C_2H_4				
1.402E+00	2.180E-04	1.581E-01	-5.900E-05	5.735E+02	-1.680E-04	5.323E-01	6.500E-05
1.097E+00	-2.000E-05	1.074E+00	-2.430E-04	5.827E+02	-7.570E-04	6.412E-01	2.780E-04
4.788E-03	2.200E-05	-8.141E-02	1.740E-04	5.647E+02	-1.436E-03	5.878E-01	4.300E-05
2.583E-02	8.400E-05	5.348E-01	-4.990E-04	5.589E+02	-1.700E-05	9.880E-01	1.310E-03
5.137E-02	2.000E-06	3.346E-01	1.310E-04	5.606E+02	1.781E-03	1.162E+00	1.830E-04
4.507E-01	-1.710E-04	-8.871E-01	3.400E-05	5.728E+02	3.900E-04	8.574E-01	1.964E-03
1.191E-01	6.700E-04	-1.034E+00	9.980E-04	5.761E+02	-1.159E-03	1.730E-01	3.775E-03
			C_2H_6				
5.959E-01	2.900E-04	-6.975E-01	-3.690E-04	5.625E+02	-6.970E-04	5.839E-01	2.740E-04
1.009E-02	7.000E-06	-6.412E-01	-3.140E-04	5.721E+02	-2.031E-03	2.404E+00	-3.030E-04
2.081E-01	3.650E-04	3.188E-01	-5.390E-04	5.620E+02	-2.700E-05	1.059E+00	1.416E-03
1.194E-02	2.160E-04	7.597E-01	-6.760E-04	5.830E+02	-4.470E-04	3.370E+00	-6.000E-05
9.358E-01	-1.800E-05	-4.891E-01	2.100E-05	5.786E+02	2.290E-04	1.382E+00	2.700E-03
			C_3H_8				
7.461E-01	5.200E-04	1.970E-01	-9.080E-04	5.581E+02	-3.300E-05	6.063E-01	2.210E-04
1.756E-01	-1.010E-04	9.958E-01	-2.200E-05	5.670E+02	-5.620E-04	7.105E-01	1.840E-04
2.154E-01	5.470E-04	8.590E-01	-1.015E-03	5.634E+02	2.360E-04	8.344E-01	1.932E-03
1.356E+00	-4.520E-04	-1.192E+00	1.449E-03	5.783E+02	-1.167E-03	1.335E+00	6.980E-04
-8.516E-02	5.530E-04	1.102E+00	-2.114E-03	5.831E+02	2.820E-04	3.126E+00	1.388E-03
1.706E-01	9.700E-05	-1.056E+00	2.400E-04	5.726E+02	-1.500E-05	2.343E+00	1.600E-04
			CH_4				
3.298E-02	5.500E-05	-1.010E+00	7.100E-05	5.799E+02	3.730E-04	5.446E-01	2.360E-04
2.167E-01	-9.900E-05	-5.988E-02	1.040E-04	5.815E+02	2.938E-03	2.270E+00	-2.600E-05
3.765E-02	9.400E-05	-3.406E-01	7.550E-04	5.865E+02	1.917E-03	2.627E+00	1.005E-03
			CH_3OCH_3				
5.938E-01	1.910E-04	-4.230E-01	-7.230E-04	5.606E+02	-8.770E-04	7.380E-01	4.230E-04
3.700E-05	0.000E+00	-3.418E-01	-3.440E-04	5.835E+02	1.072E-03	1.975E+00	3.070E-04
1.152E+00	-7.410E-04	-5.072E-01	1.380E-04	5.777E+02	-3.500E-05	1.037E+00	8.130E-04
2.158E-01	2.100E-04	-1.127E+00	4.490E-04	5.685E+02	-1.913E-03	1.728E+00	1.881E-03
5.067E-03	1.206E-03	-2.864E-01	2.490E-04	5.809E+02	-2.237E-03	3.686E+00	1.521E-03

Table 4. Basis function dependent variable coefficients within the unfiltered C–H rovibrational stretch region (~2500 – 3500 cm^{-1} Raman shift) for all hydrocarbons.

$A_{0,i}$	$A_{1,i}$	$\alpha_{0,i}$	$\alpha_{1,i}$	$\mu_{0,i}$	$\mu_{1,i}$	$\omega_{0,i}$	$\omega_{1,i}$
			C_2H_2				
1.061E-01	-2.100E-05	1.270E+00	-2.734E-03	6.301E+02	1.454E-03	6.983E-01	1.260E-04
6.591E-01	-1.040E-04	-9.208E-01	-1.300E-04	6.492E+02	-6.260E-04	4.658E-01	6.980E-04
1.387E-01	2.460E-04	8.345E-01	-1.157E-03	6.471E+02	-1.003E-03	1.207E+00	2.419E-03
1.462E-01	-4.200E-05	1.460E+00	-1.166E-03	6.491E+02	3.577E-03	9.921E-01	1.952E-03
			C_2H_4				
3.619E+00	-3.390E-04	-9.802E-01	-2.500E-05	6.349E+02	-6.100E-04	5.549E-01	2.710E-04
1.977E-01	2.240E-04	-9.537E-01	5.320E-04	6.298E+02	-1.193E-03	1.064E+00	1.027E-03
7.502E-02	1.790E-04	1.158E-01	-2.120E-04	6.428E+02	5.060E-04	1.917E+00	-7.900E-05
1.058E+00	2.900E-04	-4.882E-01	-5.510E-04	6.364E+02	-2.299E-03	2.589E+00	2.650E-04
9.261E-02	1.050E-04	-1.386E-01	8.180E-04	6.415E+02	-9.200E-04	1.801E+00	1.730E-03
1.572E+00	-1.760E-04	-7.339E-01	1.269E-03	6.387E+02	-1.218E-03	1.909E+00	1.440E-03
			C_2H_6				
3.196E+00	5.290E-04	-4.727E-01	7.940E-04	6.321E+02	-9.990E-04	4.887E-01	1.920E-04
3.504E+00	-3.950E-04	-5.743E-01	2.370E-04	6.299E+02	-2.170E-04	4.745E-01	4.710E-04
4.082E-01	4.110E-04	-1.238E+00	1.522E-03	6.252E+02	-2.107E-03	1.247E+00	2.640E-04
3.882E-02	1.040E-03	7.282E-01	-2.020E-04	6.291E+02	-2.744E-03	2.181E+00	-4.180E-04
5.270E+00	-1.780E-03	-5.101E-01	8.090E-04	6.328E+02	-7.510E-04	2.332E+00	1.620E-03
			C_3H_8				
2.685E+00	-2.780E-04	1.253E+00	-6.180E-04	6.285E+02	1.470E-04	6.604E-01	4.000E-06
1.498E+01	-6.913E-03	-2.643E-01	-5.140E-04	6.314E+02	7.400E-05	1.891E+00	-5.470E-04
-6.001E-01	2.557E-03	5.576E-01	5.340E-04	6.265E+02	3.590E-04	1.738E+00	-3.820E-04
5.772E-01	7.030E-04	9.999E-01	-2.000E-06	6.222E+02	-7.000E-06	1.527E+00	7.780E-04
-7.009E-01	3.808E-03	9.005E-01	-2.643E-03	6.389E+02	-2.237E-03	4.925E+00	5.720E-04
2.823E-01	8.800E-05	1.280E+00	-1.682E-03	6.160E+02	1.875E-03	3.797E+00	-1.198E-03
			CH_4				
4.568E+00	-7.000E-06	5.451E-01	-8.920E-04	6.301E+02	1.580E-04	4.515E-01	2.050E-04
2.501E-01	4.330E-04	2.834E-01	-6.700E-04	6.343E+02	-2.060E-04	2.771E-01	5.610E-04
4.792E-02	1.010E-04	-4.243E-01	9.820E-04	6.178E+02	-1.290E-03	8.502E-01	5.810E-04
9.198E-01	1.040E-04	9.341E-01	-1.240E-03	6.293E+02	-1.553E-03	2.395E+00	-1.034E-03
3.919E-01	-2.570E-04	8.766E-02	-1.404E-03	6.371E+02	5.600E-05	1.100E+00	-9.000E-05
1.722E-01	1.540E-04	-2.469E-01	9.990E-04	6.426E+02	2.004E-03	2.391E+00	-3.900E-05
1.364E-02	-6.000E-06	-8.630E-01	8.620E-04	6.398E+02	1.405E-03	2.826E+00	-1.146E-03
1.390E+00	-8.070E-04	2.160E-01	8.760E-04	6.359E+02	2.713E-03	3.452E+00	-1.165E-03
			CH_3OCH_3				
4.276E+00	-3.326E-03	-1.001E+00	4.000E-06	6.268E+02	-1.230E-04	5.787E-01	1.610E-04
2.620E+00	-1.572E-03	9.908E-01	1.100E-05	6.332E+02	-7.330E-04	8.446E-01	2.520E-04
1.729E+00	4.059E-03	-1.058E+00	2.900E-04	6.294E+02	-1.224E-03	9.049E-01	1.802E-03
2.656E+00	2.340E-04	-1.010E+00	5.500E-05	6.320E+02	-5.470E-04	1.237E+00	-5.700E-05
5.137E-01	3.030E-04	-2.581E-02	2.840E-04	6.211E+02	-1.954E-03	4.441E+00	-4.180E-04
8.687E-01	9.980E-04	-1.010E+00	7.700E-05	6.370E+02	1.950E-04	4.730E+00	-9.000E-04
			CH_2O				

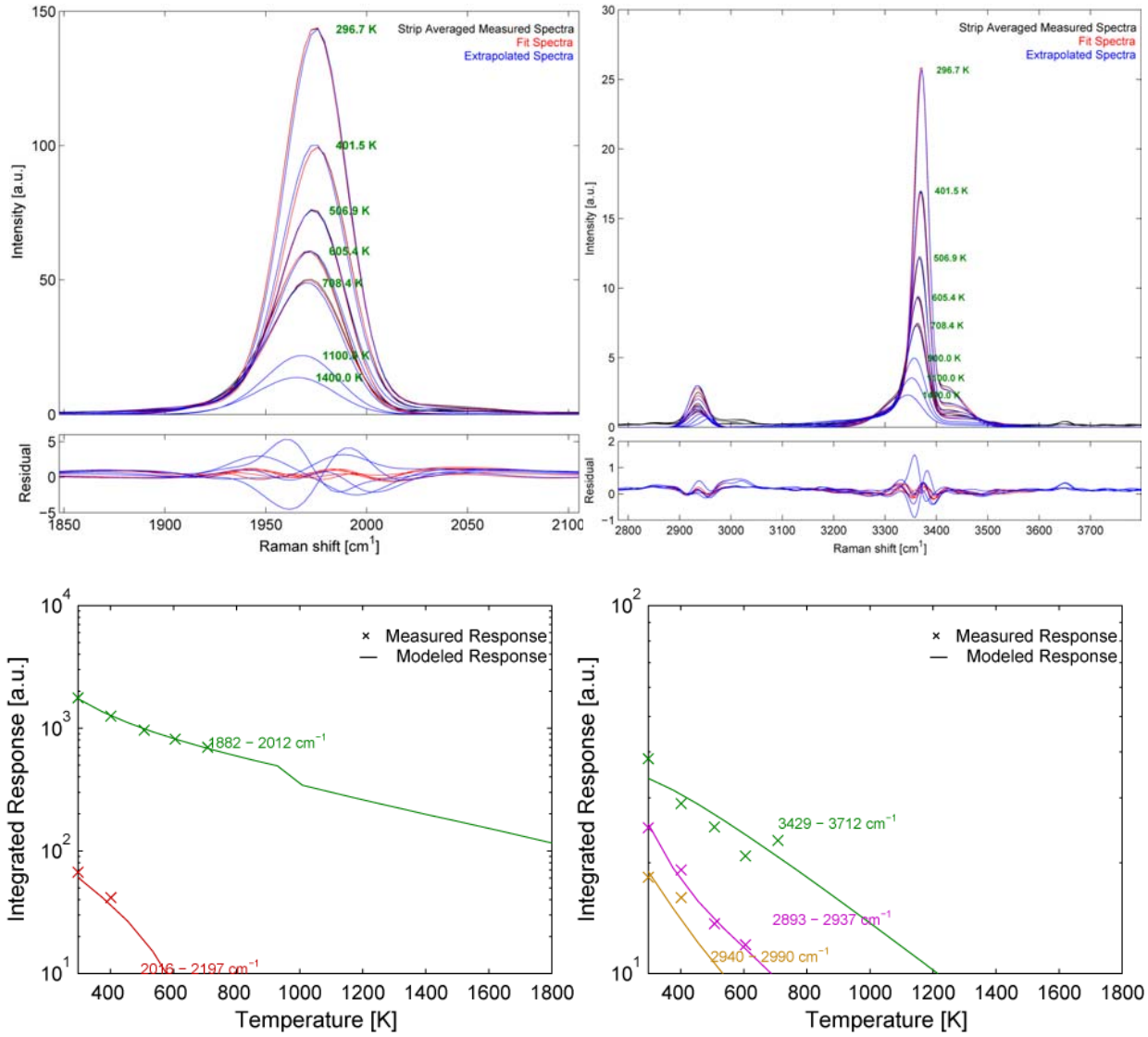

Figure 16. Reference (black), fit (red), and extrapolated (blue) spectra for the unfiltered acetylene (C_2H_2) Raman spectral data (top), along with the measured (symbols) and modeled (solid line) integrated response (bottom).

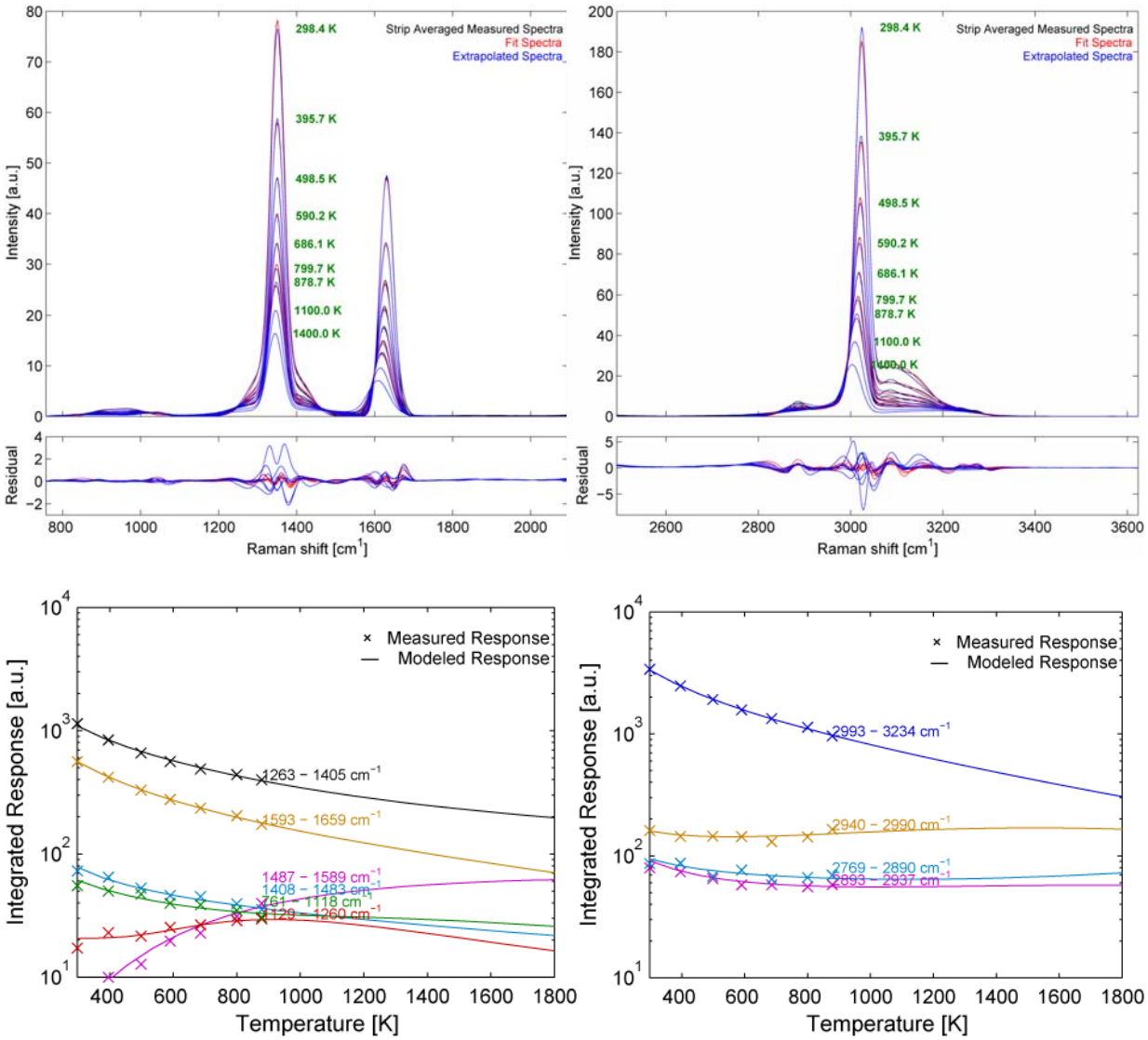

Figure 17. Reference (black), fit (red), and extrapolated (blue) spectra for the unfiltered ethylene (C_2H_4) Raman spectral data (top), along with the measured (symbols) and modeled (solid line) integrated response (bottom).

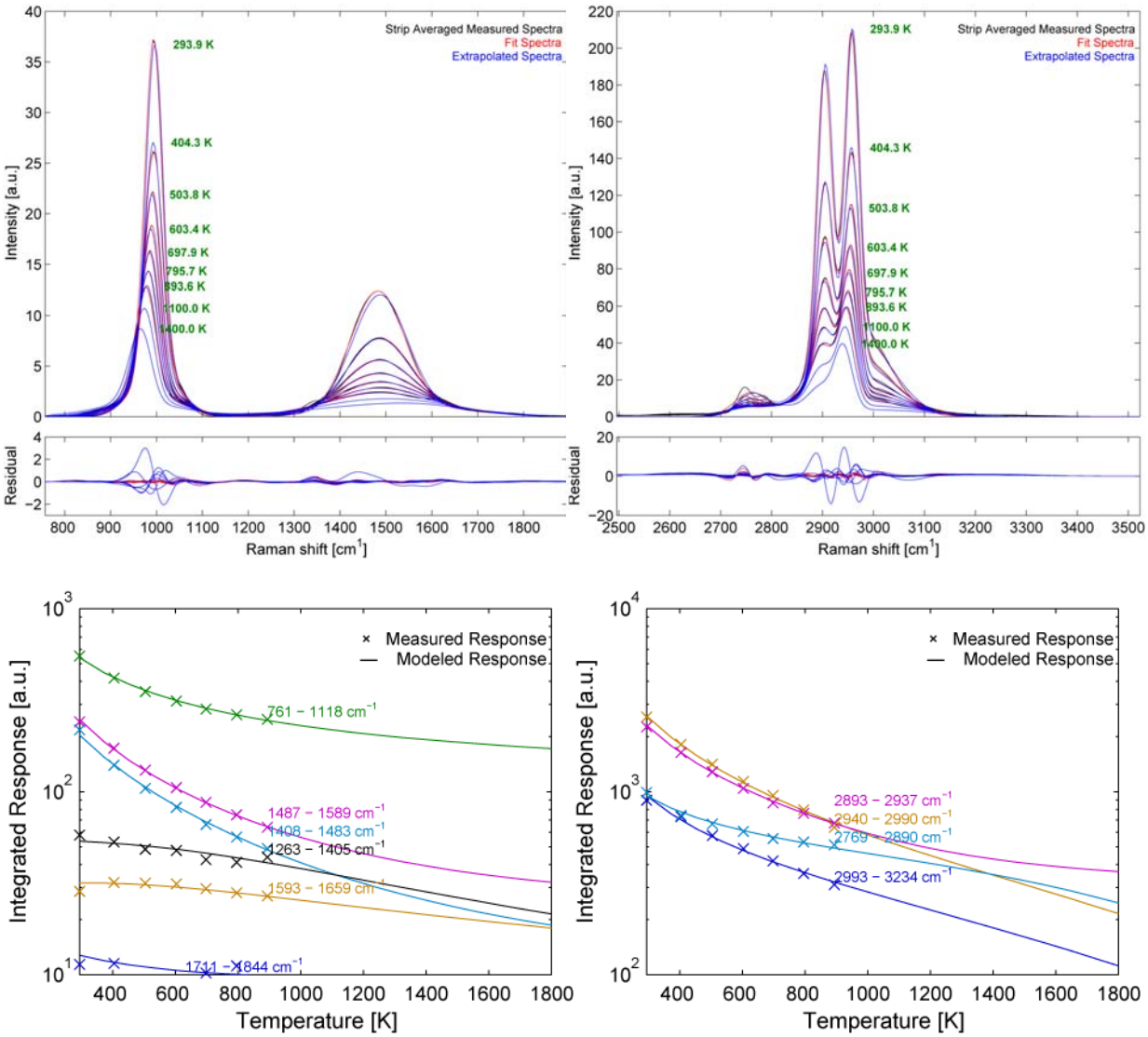

Figure 18. Reference (black), fit (red), and extrapolated (blue) spectra for the unfiltered ethane (C_2H_6) Raman spectral data (top), along with the measured (symbols) and modeled (solid line) integrated response (bottom).

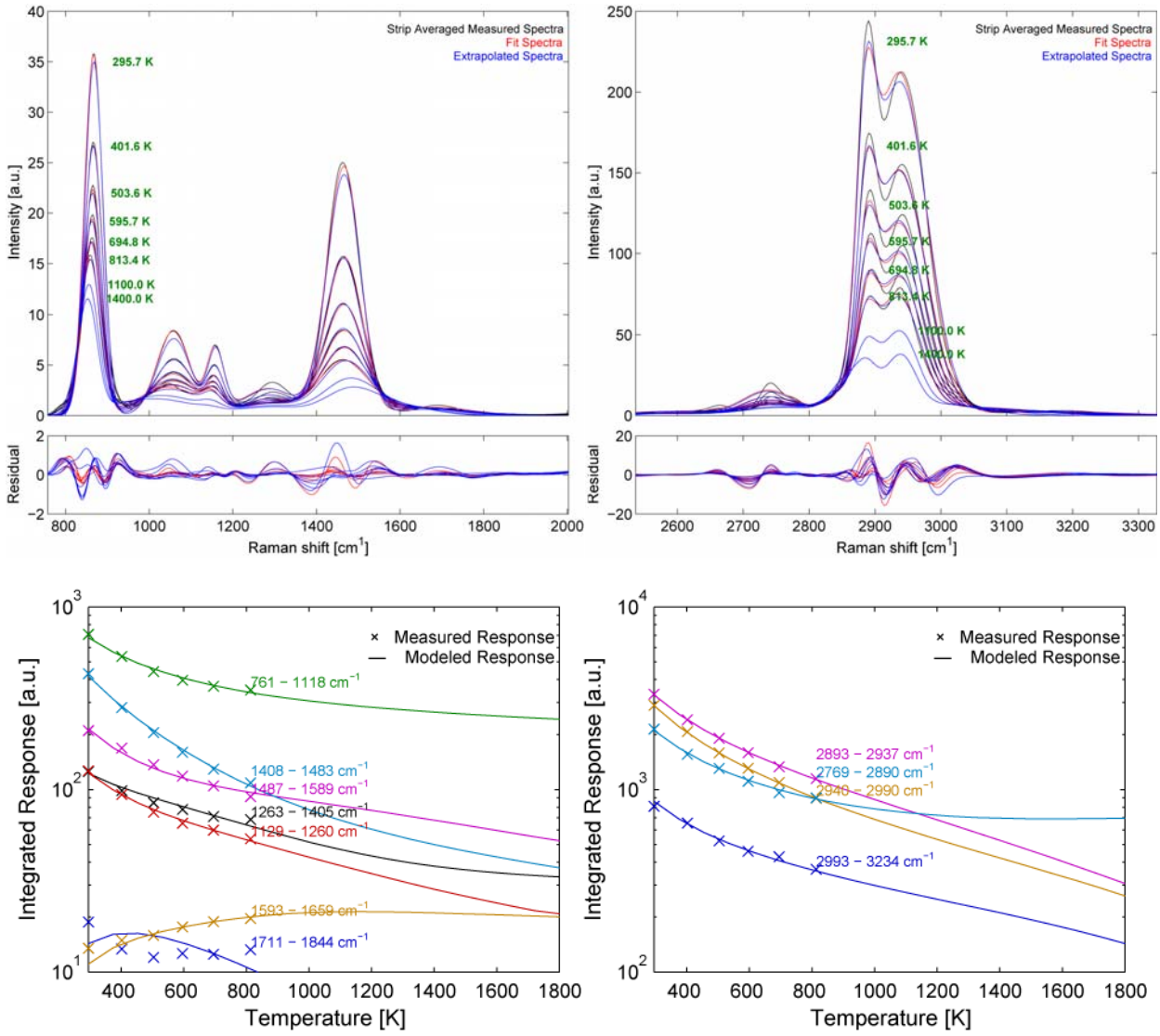

Figure 19. Reference (black), fit (red), and extrapolated (blue) spectra for the unfiltered propane (C_3H_8) Raman spectral data (top), along with the measured (symbols) and modeled (solid line) integrated response (bottom).

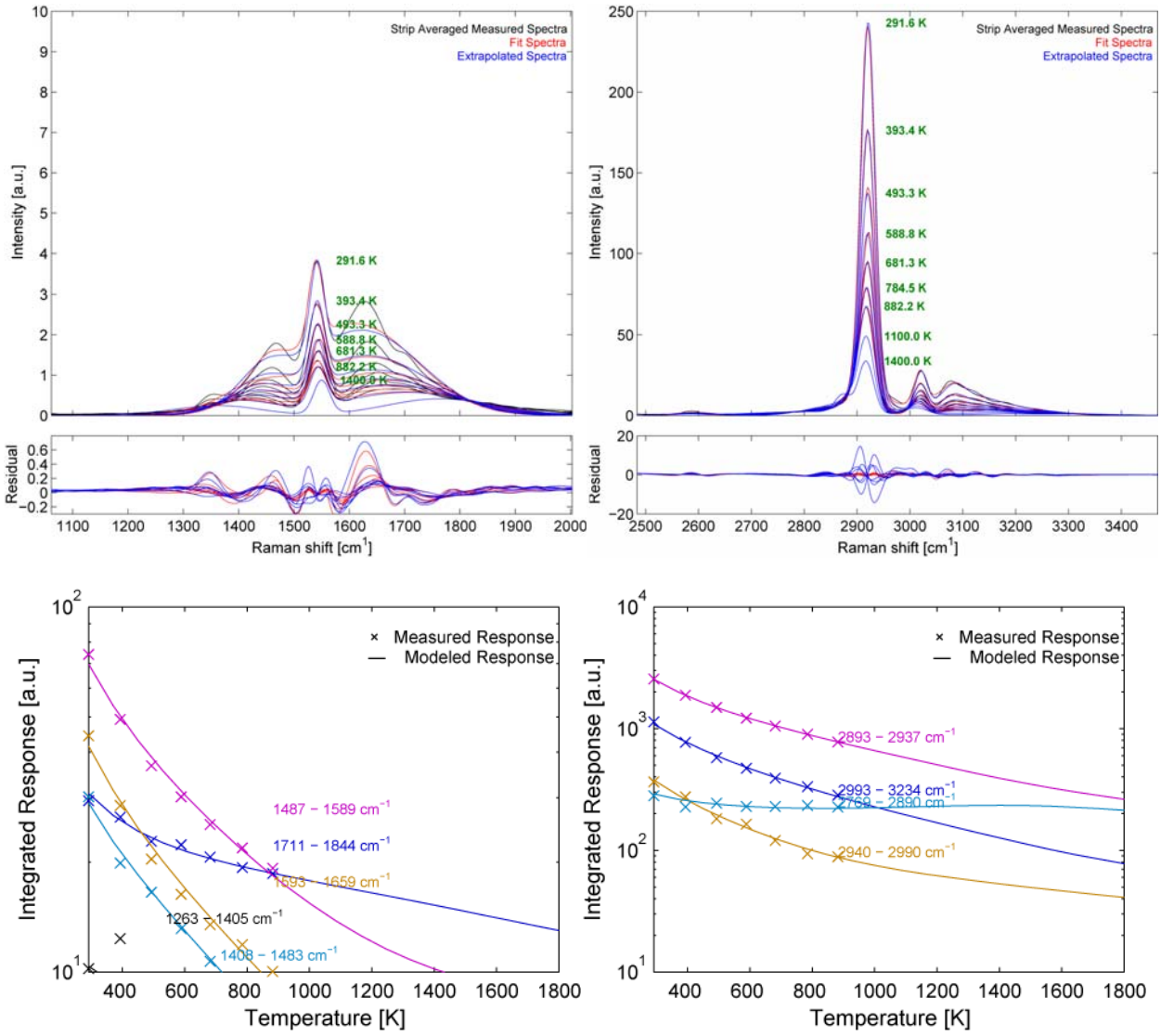

Figure 20. Reference (black), fit (red), and extrapolated (blue) spectra for the unfiltered methane (CH_4) Raman spectral data (top), along with the measured (symbols) and modeled (solid line) integrated response (bottom).

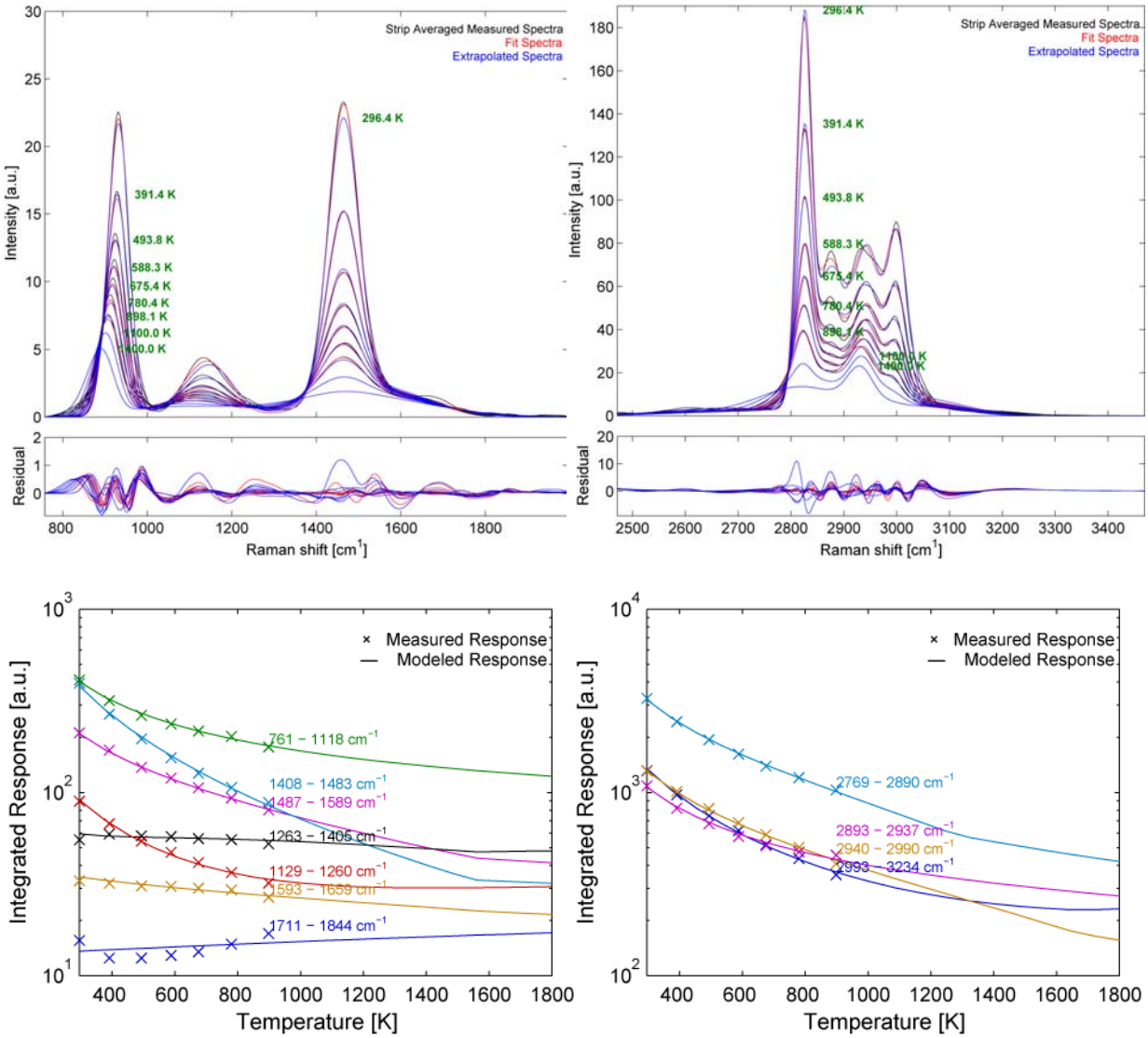

Figure 21. Reference (black), fit (red), and extrapolated (blue) spectra for the unfiltered DME (CH_3OCH_3) Raman spectral data (top), along with the measured (symbols) and modeled (solid line) integrated response (bottom).

Table 5. Basis function dependent variable coefficients within the s-polarized C–C rovibrational stretch region (~500 – 2000 cm^{-1} Raman shift) for all hydrocarbons.

$A_{0,i}$	$A_{1,i}$	$\alpha_{0,i}$	$\alpha_{1,i}$	$\mu_{0,i}$	$\mu_{1,i}$	$\omega_{0,i}$	$\omega_{1,i}$
			C_2H_2				
3.316E+00	-6.650E-04	-8.181E-01	-2.490E-04	5.953E+02	-4.560E-04	5.284E-01	3.320E-04
-7.414E-02	6.110E-04	1.099E+00	-1.383E-03	5.937E+02	-5.590E-04	1.274E+00	-7.510E-04
2.641E-02	-1.200E-05	9.845E-01	-8.000E-05	5.966E+02	4.780E-04	7.197E-01	1.630E-04
			C_2H_4				
1.120E+00	2.550E-04	-4.946E-01	-4.980E-04	5.737E+02	3.400E-05	5.524E-01	1.770E-04
9.350E-01	-1.000E-06	1.532E+00	-1.300E-03	5.824E+02	-1.380E-04	6.730E-01	1.960E-04
8.488E-03	-2.000E-06	-9.575E-01	1.861E-03	5.634E+02	-3.670E-04	9.646E-01	-5.170E-04
6.635E-02	8.100E-05	9.683E-01	-8.560E-04	5.741E+02	2.555E-03	3.446E-01	2.647E-03
5.244E-02	2.600E-05	-1.034E+00	6.760E-04	5.616E+02	1.200E-04	2.843E+00	8.900E-05
2.379E-01	1.490E-04	-2.105E-01	4.690E-04	5.733E+02	-1.428E-03	1.046E+00	2.049E-03
			C_2H_6				
4.889E-01	2.530E-04	-1.135E+00	5.770E-04	5.628E+02	-1.141E-03	6.534E-01	1.280E-04
8.526E-03	-4.000E-06	-1.159E+00	3.980E-04	5.738E+02	-1.550E-04	1.074E+00	-1.350E-04
9.549E-02	1.920E-04	4.259E-01	-8.580E-04	5.618E+02	4.550E-04	9.955E-01	1.583E-03
3.576E-02	9.700E-05	-4.559E-01	6.520E-04	5.829E+02	-4.470E-04	2.737E+00	1.820E-04
4.373E-01	3.300E-05	-6.382E-01	-1.320E-04	5.787E+02	6.300E-04	1.271E+00	3.053E-03
			C_3H_8				
5.576E-01	3.880E-04	2.476E-01	-3.500E-04	5.580E+02	-3.100E-04	6.381E-01	6.000E-05
1.390E-01	-9.700E-05	6.887E-01	4.060E-04	5.671E+02	-6.380E-04	7.074E-01	3.000E-05
5.648E-02	4.390E-04	7.955E-01	-7.040E-04	5.633E+02	3.340E-04	5.176E-01	2.980E-03
-1.028E-02	1.780E-04	3.609E-01	-5.960E-04	5.829E+02	5.280E-04	2.981E+00	7.000E-06
6.575E-01	-1.280E-04	6.879E-01	-9.000E-04	5.767E+02	7.640E-04	1.047E+00	1.139E-03
1.203E-01	8.000E-06	-5.203E-01	4.470E-04	5.718E+02	2.500E-05	2.552E+00	-9.300E-05
			CH_4				
1.318E-02	2.200E-05	-1.019E+00	9.490E-04	5.800E+02	-7.100E-05	4.420E-01	1.260E-04
2.235E-02	2.900E-05	-1.107E-02	-5.060E-04	5.774E+02	-1.642E-03	9.092E-01	1.824E-03
1.346E-01	-3.000E-06	-3.207E-01	5.600E-04	5.823E+02	2.909E-03	3.143E+00	5.430E-04
			CH_3OCH_3				
4.098E-01	8.800E-05	-5.957E-01	-5.160E-04	5.607E+02	-1.080E-03	7.451E-01	2.550E-04
4.865E-02	1.570E-04	-1.221E-01	2.370E-04	5.822E+02	4.550E-04	2.369E+00	7.000E-06
3.253E-02	-3.000E-06	-8.968E-01	2.217E-03	5.733E+02	-1.368E-03	2.962E+00	-2.005E-03
5.617E-01	-4.200E-05	1.049E+00	-1.114E-03	5.765E+02	5.780E-04	1.130E+00	9.970E-04
5.397E-02	2.690E-04	-3.712E-02	-2.800E-05	5.673E+02	-1.977E-03	4.841E-01	4.480E-03

Table 6. Basis function dependent variable coefficients within the s-polarized C–H rovibrational stretch region (~2500 – 3500 cm^{-1} Raman shift) for all hydrocarbons.

$A_{0,i}$	$A_{1,i}$	$\alpha_{0,i}$	$\alpha_{1,i}$	$\mu_{0,i}$	$\mu_{1,i}$	$\omega_{0,i}$	$\omega_{1,i}$
			C_2H_2				
5.064E-02	7.200E-05	1.582E-01	-3.120E-04	6.310E+02	-5.630E-04	6.603E-01	2.490E-04
6.062E-01	-2.700E-04	1.060E+00	-1.562E-03	6.486E+02	-6.820E-04	5.075E-01	4.130E-04
-1.169E-02	4.210E-04	1.118E+00	-1.126E-03	6.470E+02	-3.940E-04	1.915E+00	3.400E-05
			C_2H_4				
3.323E+00	-5.770E-04	3.193E-01	-3.170E-04	6.344E+02	-5.400E-04	4.855E-01	1.670E-04
1.052E-01	2.780E-04	5.134E-01	-7.450E-04	6.285E+02	6.800E-04	1.041E+00	2.950E-04
4.734E-02	1.100E-05	-6.421E-01	6.040E-04	6.443E+02	2.000E-06	9.038E-01	1.420E-04
1.293E-01	4.650E-04	-2.065E-01	-3.010E-04	6.413E+02	4.480E-04	2.144E+00	-5.000E-06
1.110E-01	8.200E-04	-8.656E-01	-1.830E-04	6.341E+02	-3.300E-04	1.405E+00	-2.800E-05
1.082E+00	-7.630E-04	2.010E-03	-1.008E-03	6.378E+02	-7.600E-05	2.019E+00	-2.570E-04
			C_2H_6				
2.864E+00	6.620E-04	-9.778E-01	1.900E-05	6.323E+02	-6.150E-04	6.098E-01	2.160E-04
3.360E+00	-9.540E-04	-5.108E-01	-4.360E-04	6.299E+02	-5.100E-05	4.690E-01	5.420E-04
4.055E-01	1.340E-04	1.412E+00	-1.602E-03	6.233E+02	-7.500E-05	1.167E+00	2.780E-04
-8.022E-02	8.720E-04	1.160E+00	-1.027E-03	6.292E+02	-2.603E-03	1.572E+00	3.580E-04
2.809E+00	-6.600E-04	-5.404E-01	6.370E-04	6.328E+02	-6.590E-04	2.459E+00	1.547E-03
			C_3H_8				
3.971E+00	-1.335E-03	-6.654E-01	1.250E-03	6.291E+02	-3.990E-04	5.962E-01	2.500E-05
-2.888E-01	2.057E-03	5.600E-01	3.620E-04	6.263E+02	1.267E-03	1.016E+00	3.700E-04
8.578E+00	-2.236E-03	9.740E-01	3.400E-05	6.302E+02	8.900E-05	1.702E+00	-5.000E-04
2.156E-02	3.300E-05	-6.269E-02	-4.450E-04	6.173E+02	-5.210E-04	1.547E+00	-7.710E-04
9.101E-02	5.400E-05	1.725E+00	-2.680E-03	6.197E+02	-8.900E-05	7.451E-01	4.510E-04
2.899E-01	6.820E-04	1.520E+00	-1.333E-03	6.225E+02	7.740E-04	7.836E-01	1.142E-03
-1.750E-01	1.009E-03	7.021E-01	-2.464E-03	6.393E+02	-2.722E-03	1.201E+00	1.965E-03
			CH_4				
4.012E+00	-6.610E-04	6.828E-02	-2.360E-04	6.302E+02	-3.000E-05	4.891E-01	7.000E-05
2.131E-01	7.300E-05	6.135E-01	-3.760E-04	6.342E+02	-3.350E-04	4.646E-01	2.370E-04
5.316E-02	2.600E-05	9.822E-01	-5.680E-04	6.170E+02	-6.400E-04	8.082E-01	4.990E-04
1.810E-01	-8.800E-05	1.016E+00	-7.300E-05	6.360E+02	2.030E-04	6.854E-01	6.400E-05
1.953E-01	7.770E-04	9.388E-01	-3.960E-04	6.300E+02	-1.318E-03	7.758E-01	1.470E-04
2.990E-01	3.930E-04	3.112E-01	-4.210E-04	6.295E+02	-2.886E-03	2.426E+00	1.190E-04
3.040E-01	-1.580E-04	-2.882E-01	4.050E-04	6.373E+02	1.461E-03	1.367E+00	1.310E-04
3.705E-01	0.000E+00	-8.574E-01	1.110E-03	6.415E+02	8.890E-04	3.347E+00	3.570E-04
2.427E-01	-9.900E-05	-7.821E-02	-1.210E-04	6.341E+02	1.657E-03	3.956E+00	1.350E-04
			CH_3OCH_3				
3.678E+00	-2.658E-03	-3.302E-01	6.220E-04	6.266E+02	-4.720E-04	5.454E-01	5.100E-05
1.770E+00	-1.133E-03	4.144E-01	-8.200E-04	6.334E+02	-1.470E-04	5.752E-01	2.400E-04
1.855E+00	3.920E-04	7.251E-01	4.300E-05	6.310E+02	-6.650E-04	1.107E+00	-2.600E-05
1.633E+00	3.265E-03	-4.303E-01	-9.300E-05	6.290E+02	-8.370E-04	8.354E-01	1.851E-03
2.158E-01	5.840E-04	-8.199E-01	-2.180E-04	6.364E+02	-5.400E-05	1.480E+00	1.194E-03
3.237E-02	2.250E-04	-1.393E-01	1.180E-04	6.420E+02	-1.339E-03	1.716E+00	1.396E-03
3.707E-01	1.840E-04	1.029E+00	-2.990E-04	6.180E+02	-7.670E-04	7.246E+00	-1.904E-03
			CH_2O				
1.012E+02	-4.991E-03	-9.996E-01	1.785E-04	6.237E+02	1.769E-04	1.946E+00	-4.840E-05
3.175E+02	-1.895E-02	9.464E-01	-5.692E-04	6.240E+02	1.225E-03	1.047E-02	1.458E-03

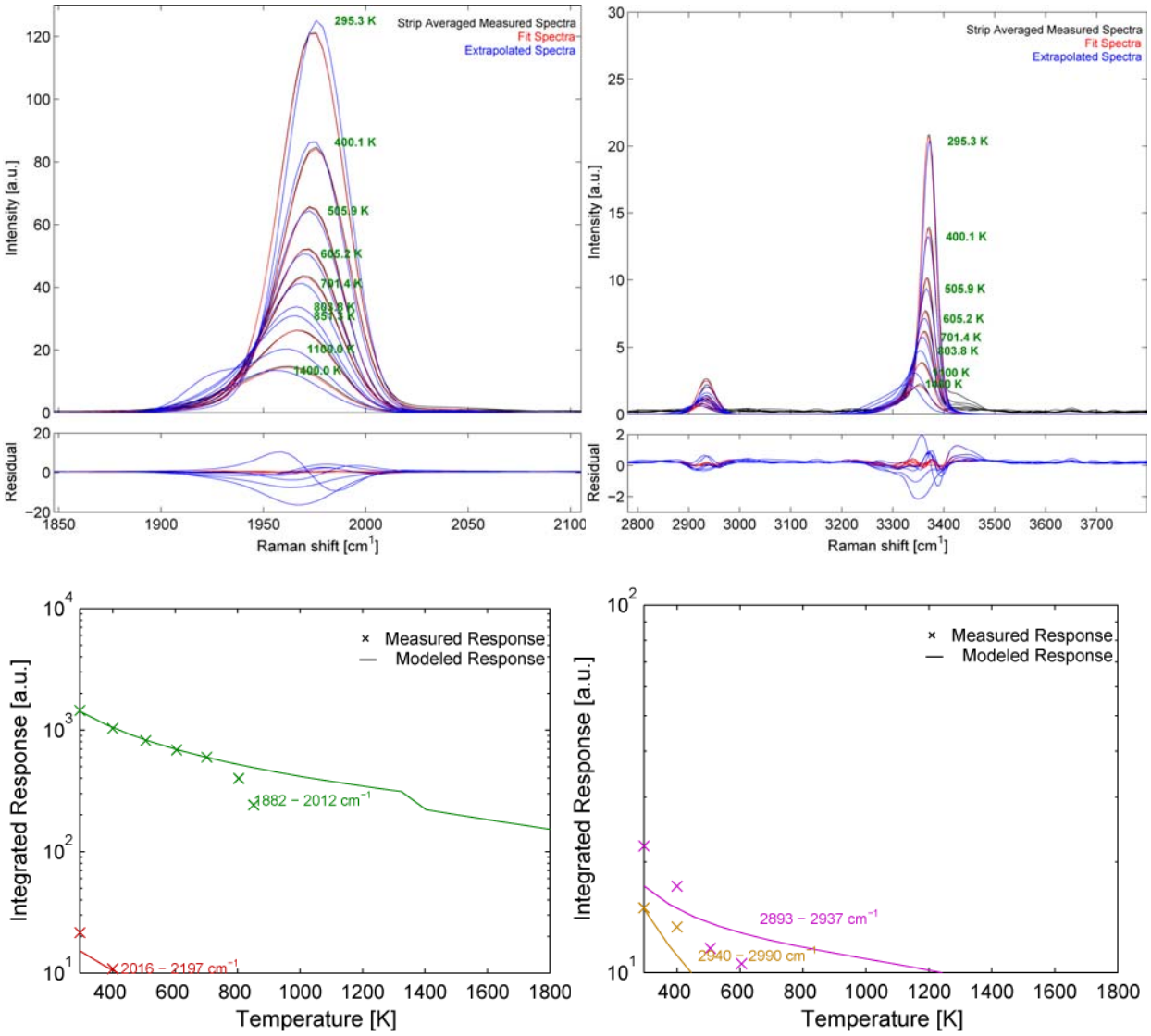

Figure 22. Reference (black), fit (red), and extrapolated (blue) spectra for the s-polarized acetylene (C_2H_2) Raman spectral data (top), along with the measured (symbols) and modeled (solid line) integrated response (bottom).

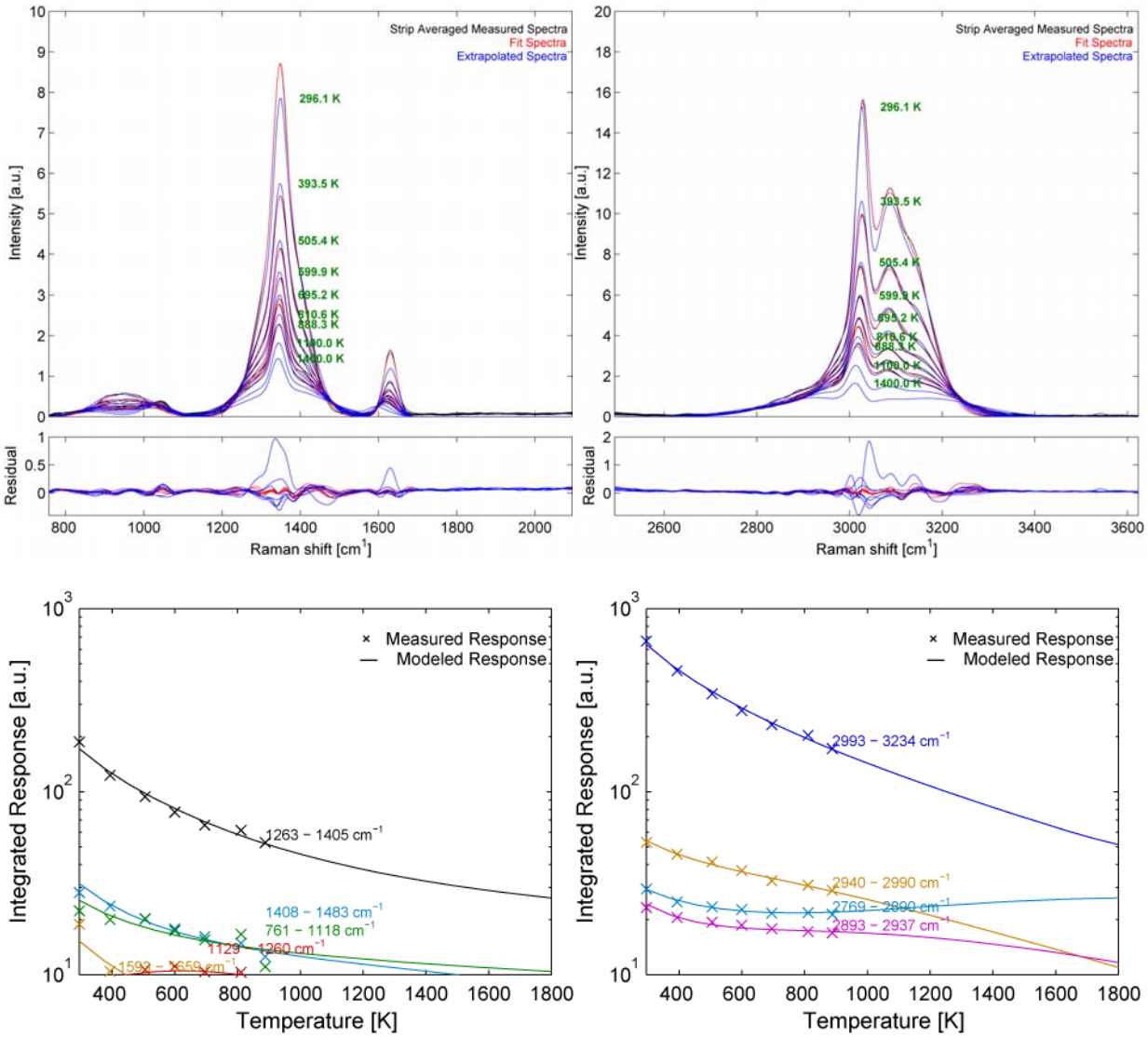

Figure 23. Reference (black), fit (red), and extrapolated (blue) spectra for the s-polarized ethylene (C_2H_4) Raman spectral data (top), along with the measured (symbols) and modeled (solid line) integrated response (bottom).

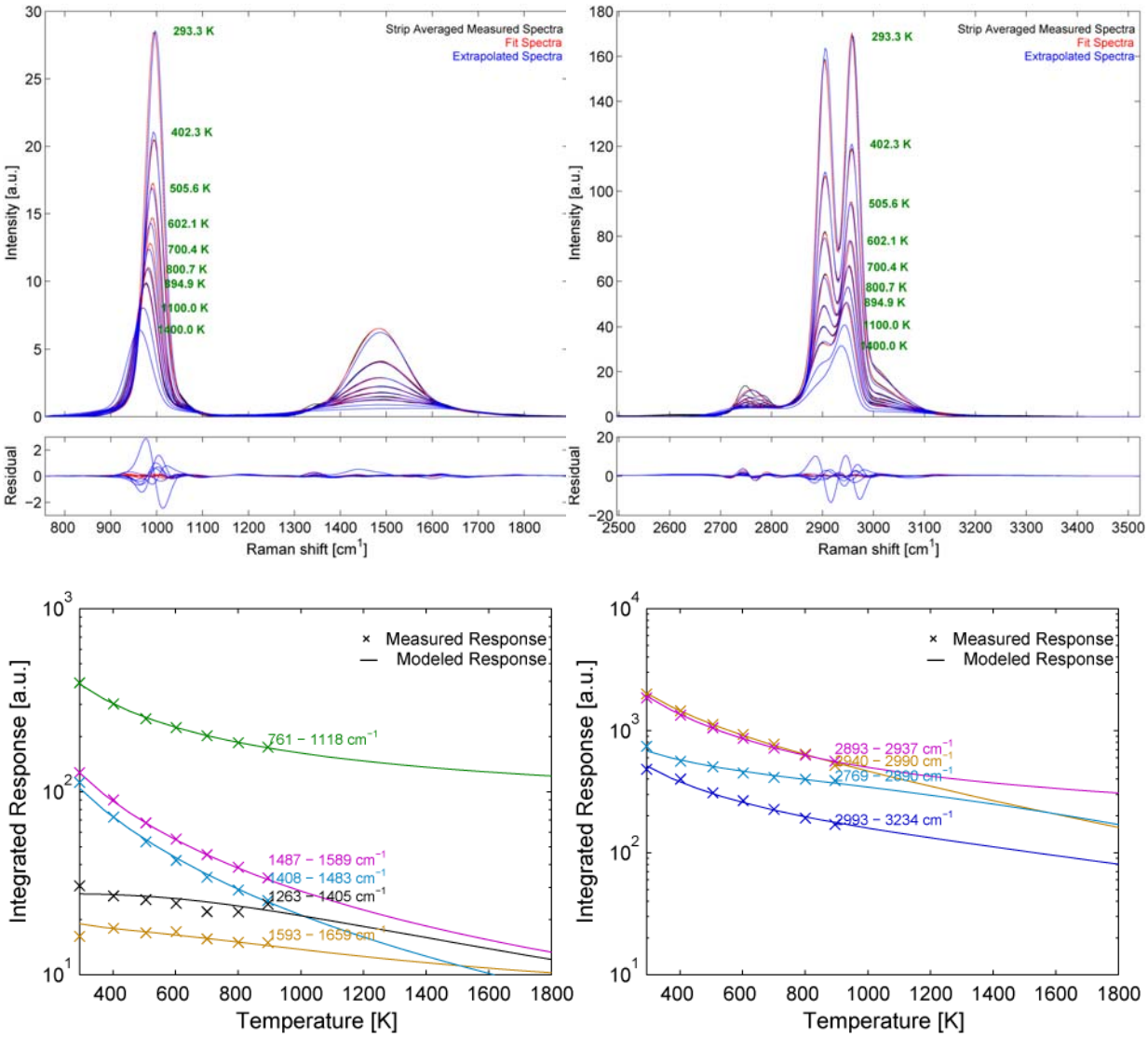

Figure 24. Reference (black), fit (red), and extrapolated (blue) spectra for the s-polarized ethane (C_2H_6) Raman spectral data (top), along with the measured (symbols) and modeled (solid line) integrated response (bottom).

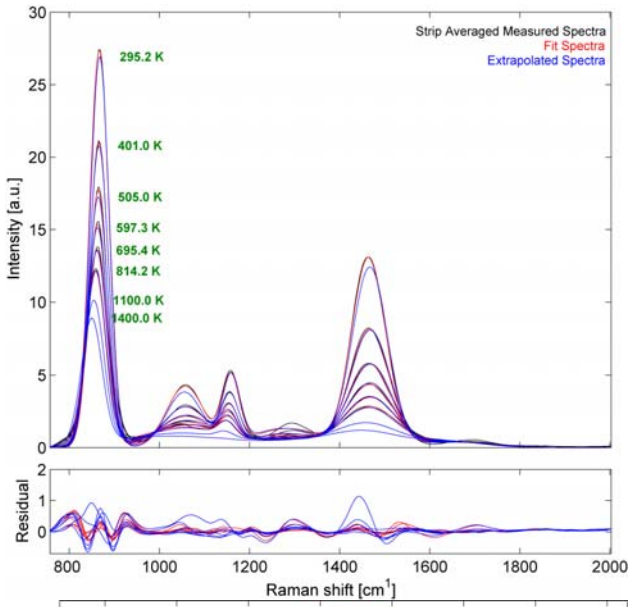
Strip Averaged Measured Spectra
Fit Spectra
Extrapolated Spectra
295.2 K
401.0 K
505.0 K
597.3 K
695.4 K
814.2 K
1100.0 K
1400.0 K
Intensity [a.u.]
Residual
Raman shift [cm^{-1}]

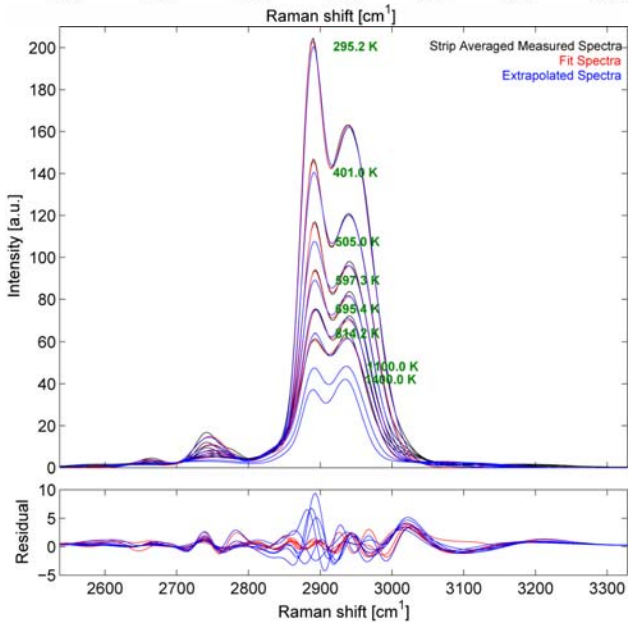
Strip Averaged Measured Spectra
Fit Spectra
Extrapolated Spectra
295.2 K
401.0 K
505.0 K
597.3 K
695.4 K
814.2 K
1100.0 K
1400.0 K
Intensity [a.u.]
Residual
Raman shift [cm^{-1}]

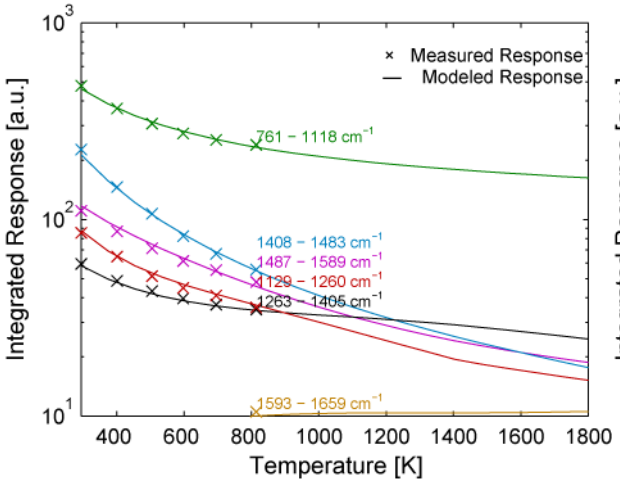
Measured Response
Modeled Response
761 – 1118 cm^{-1}
1408 – 1483 cm^{-1}
1487 – 1589 cm^{-1}
1129 – 1260 cm^{-1}
1263 – 1405 cm^{-1}
1593 – 1659 cm^{-1}
Integrated Response [a.u.]
Temperature [K]

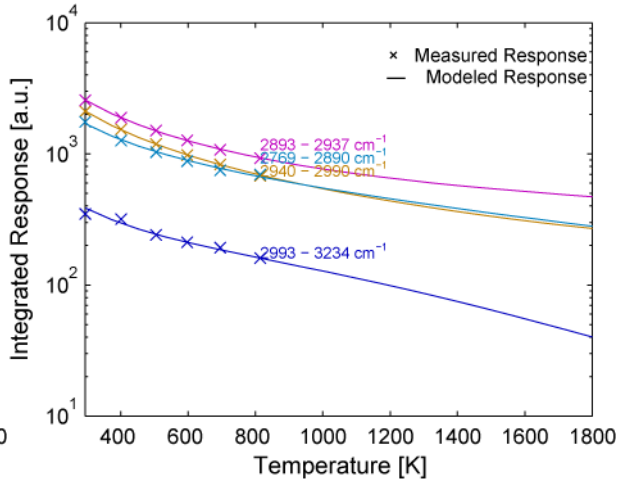
Measured Response
Modeled Response
2893 – 2937 cm^{-1}
2769 – 2890 cm^{-1}
2940 – 2990 cm^{-1}
2993 – 3234 cm^{-1}
Integrated Response [a.u.]
Temperature [K]

Figure 25. Reference (black), fit (red), and extrapolated (blue) spectra for the s-polarized propane (C_3H_8) Raman spectral data (top), along with the measured (symbols) and modeled (solid line) integrated response (bottom).

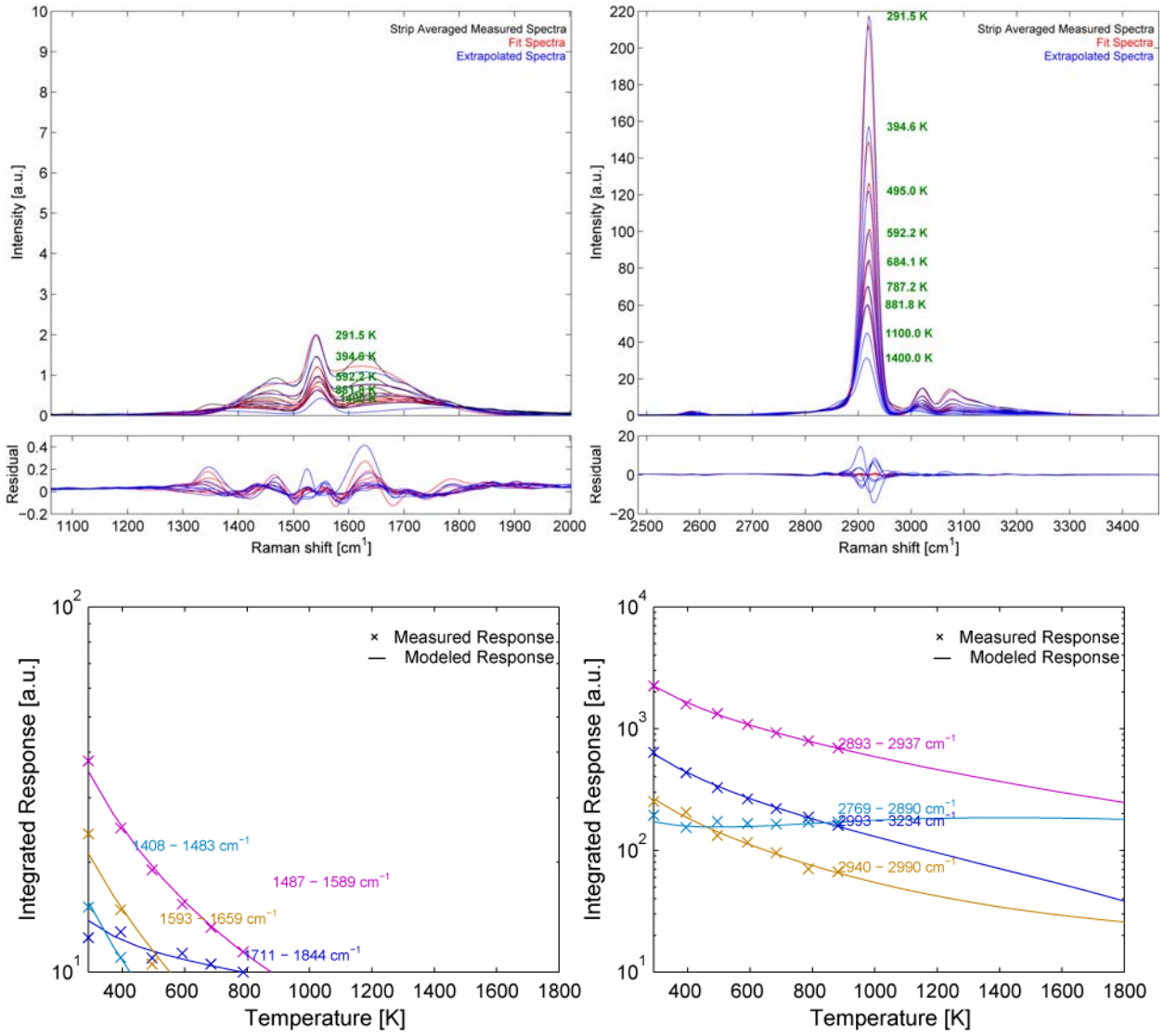

Figure 26. Reference (black), fit (red), and extrapolated (blue) spectra for the s-polarized methane (CH_4) Raman spectral data (top), along with the measured (symbols) and modeled (solid line) integrated response (bottom).

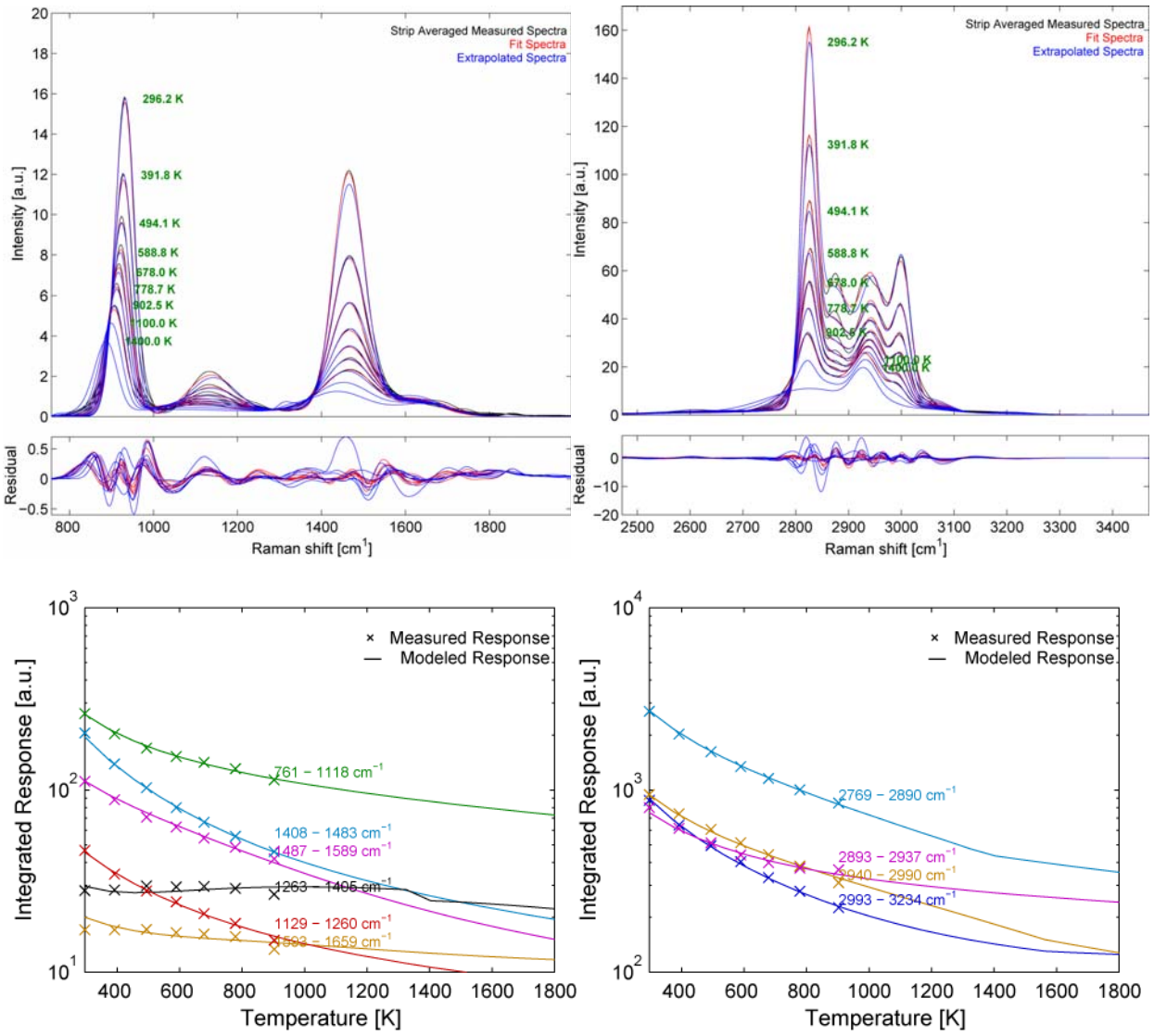

Figure 27. Reference (black), fit (red), and extrapolated (blue) spectra for the s-polarized DME (CH_3OCH_3) Raman spectral data (top), along with the measured (symbols) and modeled (solid line) integrated response (bottom).

Table 7. Basis function dependent variable coefficients within the p-polarized C–C rovibrational stretch region (~500 – 2000 cm^{-1} Raman shift) for all hydrocarbons.

$A_{0,i}$	$A_{1,i}$	$\alpha_{0,i}$	$\alpha_{1,i}$	$\mu_{0,i}$	$\mu_{1,i}$	$\omega_{0,i}$	$\omega_{1,i}$
			C_2H_2				
1.618E-01	-1.800E-05	-9.968E-01	-2.000E-06	5.953E+02	-4.300E-04	5.192E-01	3.380E-04
8.770E-02	4.700E-05	1.025E+00	-1.578E-03	5.934E+02	-1.308E-03	2.002E+00	2.000E-06
2.883E-02	9.100E-05	-9.893E-01	1.511E-03	5.975E+02	-4.040E-04	1.048E+00	1.137E-03
			C_2H_4				
2.955E-02	2.000E-06	-6.403E-01	2.203E-03	5.833E+02	-1.679E-03	4.736E-01	6.220E-04
5.809E-02	1.400E-05	1.031E+00	-4.020E-04	5.731E+02	-8.800E-05	5.796E-01	-5.000E-06
-1.131E-03	4.500E-05	-6.358E-01	7.990E-04	5.630E+02	-8.100E-05	1.296E+00	-1.700E-05
3.434E-02	3.000E-06	-8.041E-02	1.290E-04	5.605E+02	-1.963E-03	1.728E+00	1.100E-05
3.081E-01	6.100E-05	-9.977E-01	1.085E-03	5.751E+02	-1.681E-03	1.690E+00	1.296E-03
			C_2H_6				
1.199E-01	1.050E-04	6.678E-01	-9.020E-04	5.619E+02	-1.170E-04	1.246E+00	4.130E-04
3.326E-01	8.700E-05	-1.134E-01	3.670E-04	5.780E+02	-2.640E-04	1.124E+00	3.216E-03
			C_3H_8				
9.605E-02	7.500E-05	9.360E-01	-1.486E-03	5.575E+02	6.880E-04	8.486E-01	4.820E-04
1.068E-01	1.360E-04	7.610E-01	-1.250E-03	5.636E+02	6.760E-04	1.153E+00	1.124E-03
4.834E-01	-7.700E-05	-3.518E-01	3.820E-04	5.776E+02	-2.610E-04	9.236E-01	1.342E-03
1.849E-03	1.070E-04	2.289E-01	-1.180E-04	5.836E+02	-1.105E-03	2.706E+00	4.530E-04
6.670E-02	2.800E-05	-1.162E+00	4.180E-04	5.727E+02	-4.280E-04	1.916E+00	5.780E-04
			CH_4				
1.261E-02	3.000E-06	9.998E-01	0.000E+00	5.794E+02	1.950E-04	5.635E-01	0.000E+00
1.413E-02	-1.100E-05	-1.041E+00	1.010E-04	5.781E+02	-2.395E-03	1.205E+00	-2.000E-05
9.234E-02	7.300E-05	8.725E-02	1.320E-04	5.816E+02	4.170E-04	2.157E+00	5.754E-03
			CH_3OCH_3				
1.194E-01	7.400E-05	1.278E-01	2.130E-04	5.604E+02	-1.566E-03	6.781E-01	1.116E-03
2.785E-02	4.700E-05	2.645E-02	1.280E-04	5.829E+02	1.704E-03	1.791E+00	4.950E-04
9.548E-02	4.900E-05	1.281E+00	-1.734E-03	5.655E+02	1.258E-03	2.146E+00	2.430E-04
2.573E-02	1.400E-05	-1.261E+00	2.775E-03	5.802E+02	1.399E-03	1.402E+00	5.300E-05
3.846E-01	6.200E-05	8.515E-01	-9.730E-04	5.765E+02	5.930E-04	8.342E-01	1.701E-03

Table 8. Basis function dependent variable coefficients within the p-polarized C–H rovibrational stretch region (~2500 – 3500 cm^{-1} Raman shift) for all hydrocarbons.

$A_{0,i}$	$A_{1,i}$	$\alpha_{0,i}$	$\alpha_{1,i}$	$\mu_{0,i}$	$\mu_{1,i}$	$\omega_{0,i}$	$\omega_{1,i}$
			C_2H_2				
-1.338E-02	7.300E-05	3.606E-01	-5.200E-04	6.637E+02	-2.302E-03	1.450E+00	-1.000E-06
3.887E-02	4.000E-05	-1.354E+00	1.145E-03	6.493E+02	-1.217E-03	2.403E-01	1.085E-03
-9.971E-03	1.000E-04	-8.798E-02	5.000E-05	6.335E+02	6.190E-04	1.912E+00	0.000E+00
-4.068E-03	1.650E-04	4.857E-01	-8.430E-04	6.472E+02	-3.725E-03	2.677E+00	2.200E-05
8.720E-02	4.800E-05	-9.748E-01	1.416E-03	6.502E+02	2.815E-03	2.849E+00	-4.000E-06
			C_2H_4				
2.183E-01	-7.200E-05	1.169E+00	-1.912E-03	6.342E+02	1.430E-04	4.476E-01	3.200E-04
1.888E-01	-1.120E-04	-1.057E+00	1.270E-04	6.371E+02	-1.900E-05	1.154E+00	9.000E-05
8.619E-02	1.280E-04	9.512E-01	-9.250E-04	6.331E+02	-1.134E-03	1.146E+00	9.850E-04
6.322E-01	5.900E-05	-6.983E-01	7.700E-04	6.392E+02	-1.740E-04	1.741E+00	2.003E-03
1.890E-01	7.300E-05	3.739E-01	-6.190E-04	6.314E+02	-2.210E-03	3.649E+00	1.480E-04
			C_2H_6				
1.471E-01	-4.500E-05	1.002E+00	-1.600E-05	6.316E+02	-6.190E-04	7.881E-01	5.000E-06
1.434E-01	-4.200E-05	1.106E+00	-3.580E-04	6.293E+02	-2.860E-04	6.882E-01	4.830E-04
3.219E-02	2.300E-05	-3.717E-01	-1.900E-04	6.199E+02	-1.560E-04	2.110E+00	2.700E-05
2.627E-02	5.500E-05	9.443E-02	-8.500E-05	6.413E+02	5.490E-04	2.446E+00	-8.300E-05
1.094E-01	3.720E-04	2.153E-01	-5.320E-04	6.286E+02	-1.594E-03	3.355E+00	2.430E-04
1.712E+00	-3.230E-04	5.589E-01	-2.100E-04	6.313E+02	4.480E-04	2.014E+00	2.126E-03
			C_3H_8				
1.364E-02	-1.000E-05	1.828E+00	-2.494E-03	6.160E+02	1.291E-03	1.248E+00	-5.450E-04
4.619E-01	-5.350E-04	-9.700E-01	-3.800E-05	6.296E+02	-3.610E-04	9.620E-01	-3.000E-06
9.971E-02	1.220E-04	1.496E+00	-1.634E-03	6.278E+02	-2.898E-03	1.154E+00	1.005E-03
9.365E-02	1.800E-05	-1.130E+00	1.237E-03	6.415E+02	1.150E-03	2.601E+00	5.800E-04
1.718E-01	5.500E-05	-4.438E-01	4.730E-04	6.244E+02	-3.642E-03	3.131E+00	-4.100E-05
-7.235E-02	2.860E-04	7.301E-01	-2.108E-03	6.377E+02	1.277E-03	2.483E+00	8.290E-04
2.157E+00	1.530E-04	8.048E-01	-1.054E-03	6.310E+02	1.990E-04	1.312E+00	1.326E-03
			CH_4				
1.312E-01	5.600E-05	-9.727E-01	4.500E-04	6.347E+02	-4.740E-04	4.534E-01	2.350E-04
1.713E-01	-2.400E-05	-1.999E-01	-1.068E-03	6.306E+02	-1.900E-05	6.146E-01	2.530E-04
2.732E-01	-1.070E-04	1.002E+00	-5.000E-06	6.363E+02	1.740E-03	1.433E+00	1.023E-03
4.912E-01	-1.000E-05	1.085E+00	-1.293E-03	6.307E+02	-3.681E-03	4.760E+00	1.060E-04
1.283E-01	2.040E-04	1.030E+00	-1.060E-04	6.399E+02	4.000E-04	1.539E+00	4.827E-03
			CH_3OCH_3				
1.180E-01	-7.400E-05	1.050E+00	-1.090E-04	6.262E+02	-2.790E-04	7.913E-01	7.200E-05
2.218E-02	-3.000E-06	-1.260E+00	2.145E-03	6.418E+02	2.070E-04	2.055E+00	4.710E-04
5.006E-01	-4.000E-05	-1.070E+00	2.760E-04	6.347E+02	-1.089E-03	9.187E-01	2.073E-03
1.065E+00	1.040E-04	7.999E-01	-1.186E-03	6.293E+02	2.980E-04	1.597E+00	2.964E-03
3.613E-01	9.900E-05	-6.055E-01	1.659E-03	6.333E+02	-5.010E-04	5.394E+00	4.700E-05
1.368E-01	6.400E-05	1.035E+00	-2.340E-04	6.176E+02	-1.656E-03	4.263E+00	1.570E-04
			CH_2O				
2.077E+02	-1.275E-02	-5.662E-01	5.084E-04	6.248E+02	4.901E-04	4.080E-01	7.161E-04
4.910E+01	-2.266E-03	3.157E-02	-4.847E-04	6.226E+02	1.297E-03	2.156E-00	-6.474E-04

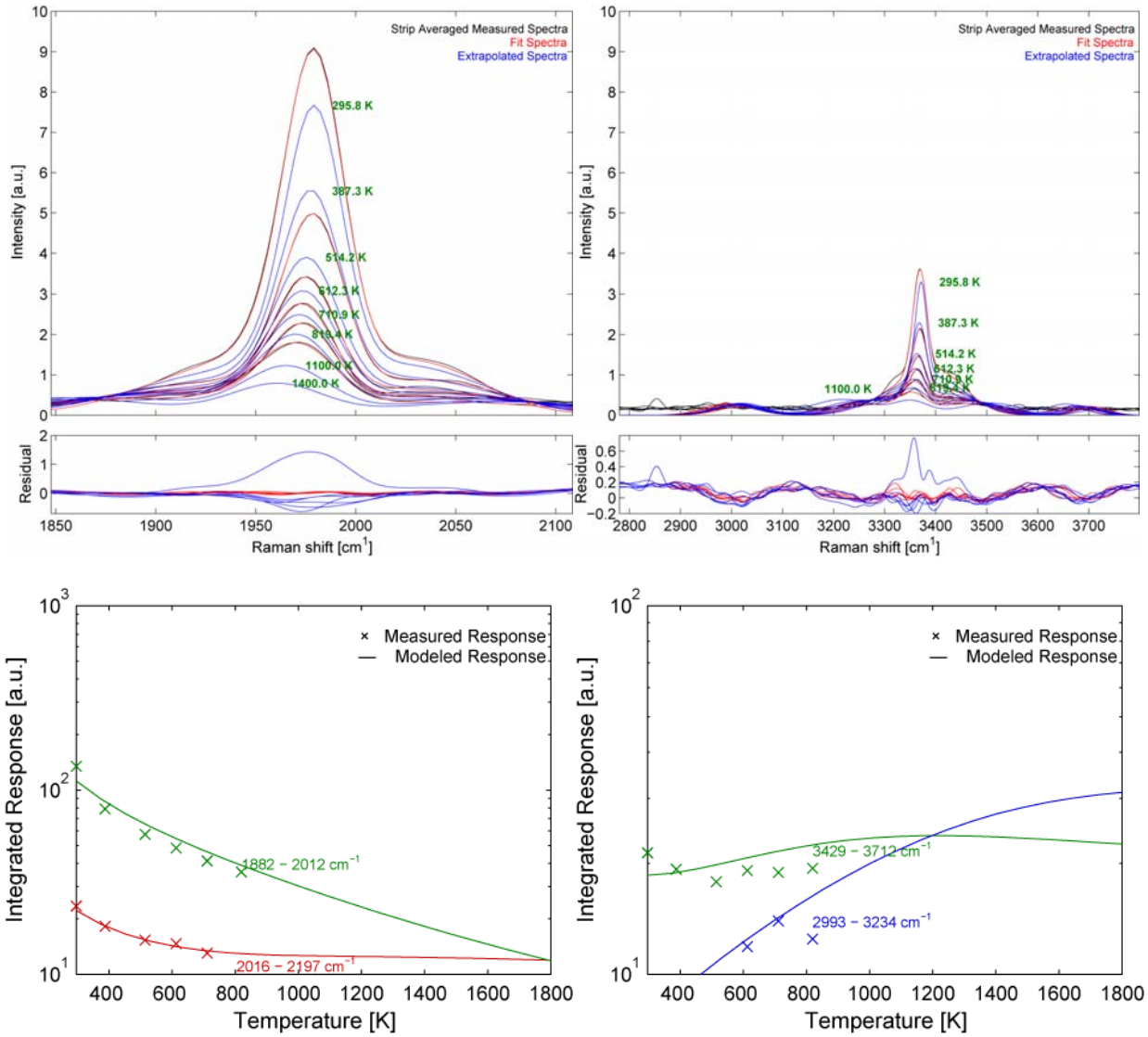

Figure 28. Reference (black), fit (red), and extrapolated (blue) spectra for the p-polarized acetylene (C_2H_2) Raman spectral data (top), along with the measured (symbols) and modeled (solid line) integrated response (bottom).

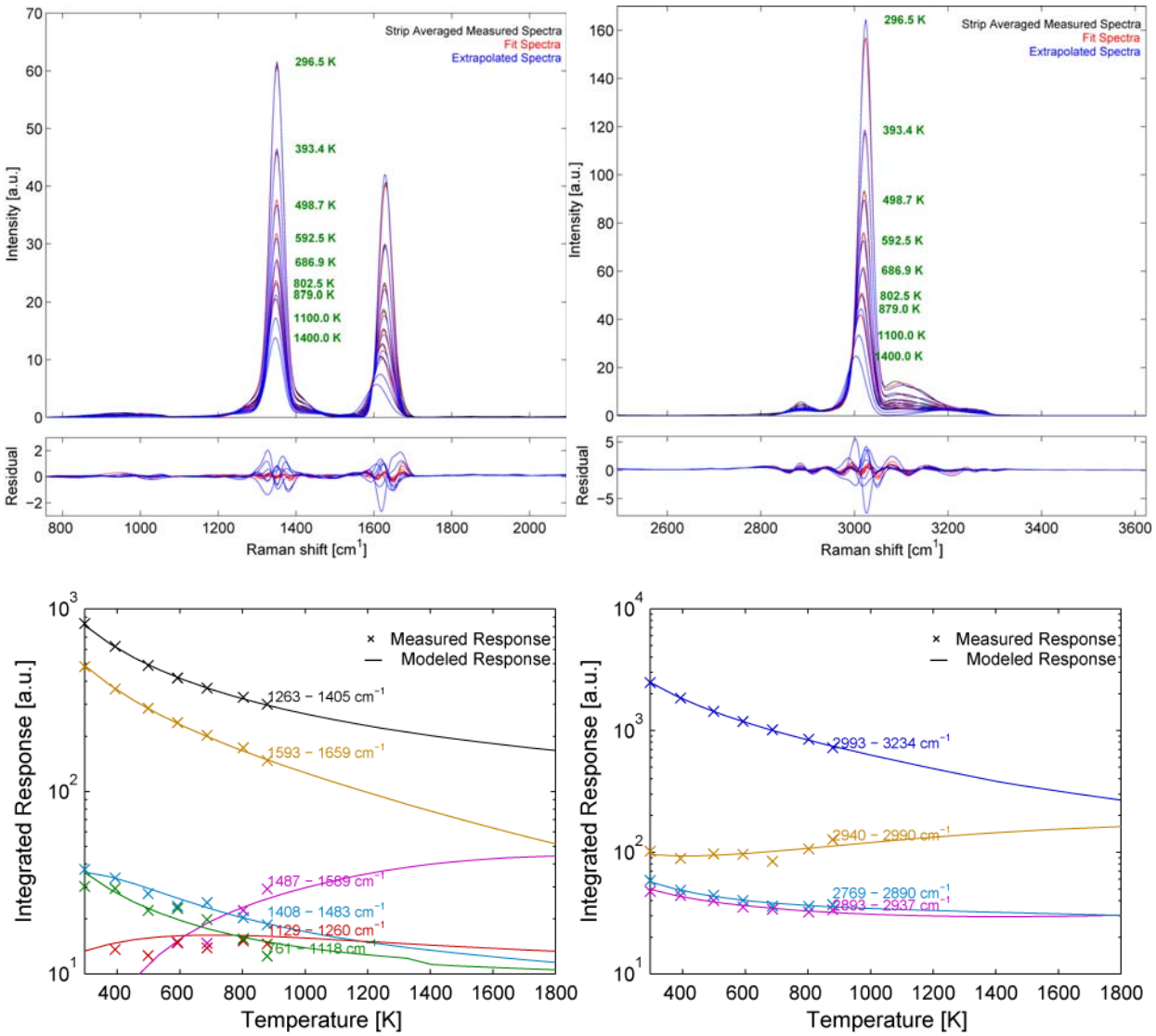

Figure 29. Reference (black), fit (red), and extrapolated (blue) spectra for the p-polarized ethylene (C_2H_4) Raman spectral data (top), along with the measured (symbols) and modeled (solid line) integrated response (bottom).

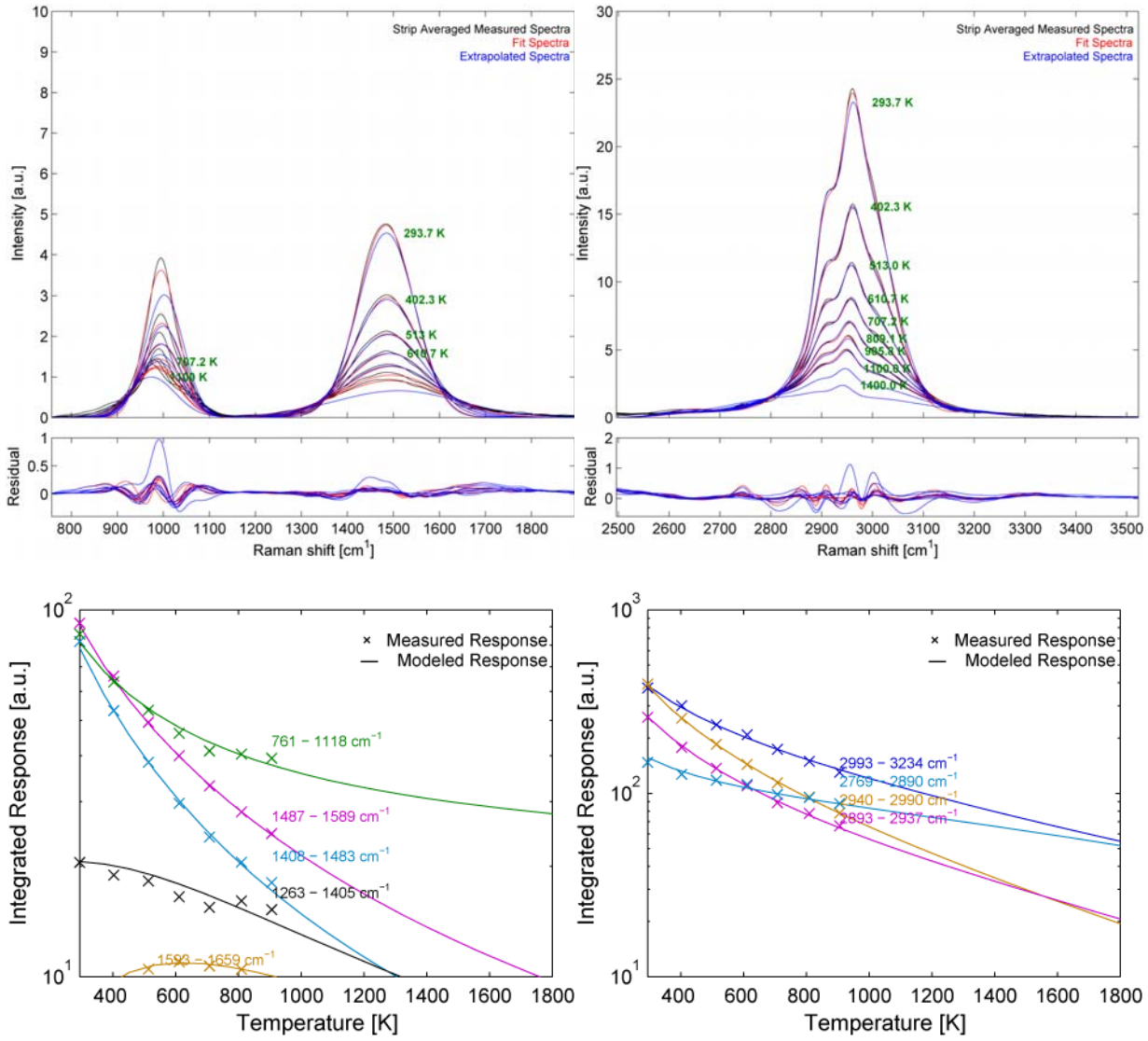

Figure 30. Reference (black), fit (red), and extrapolated (blue) spectra for the p-polarized ethane (C_2H_6) Raman spectral data (top), along with the measured (symbols) and modeled (solid line) integrated response (bottom).

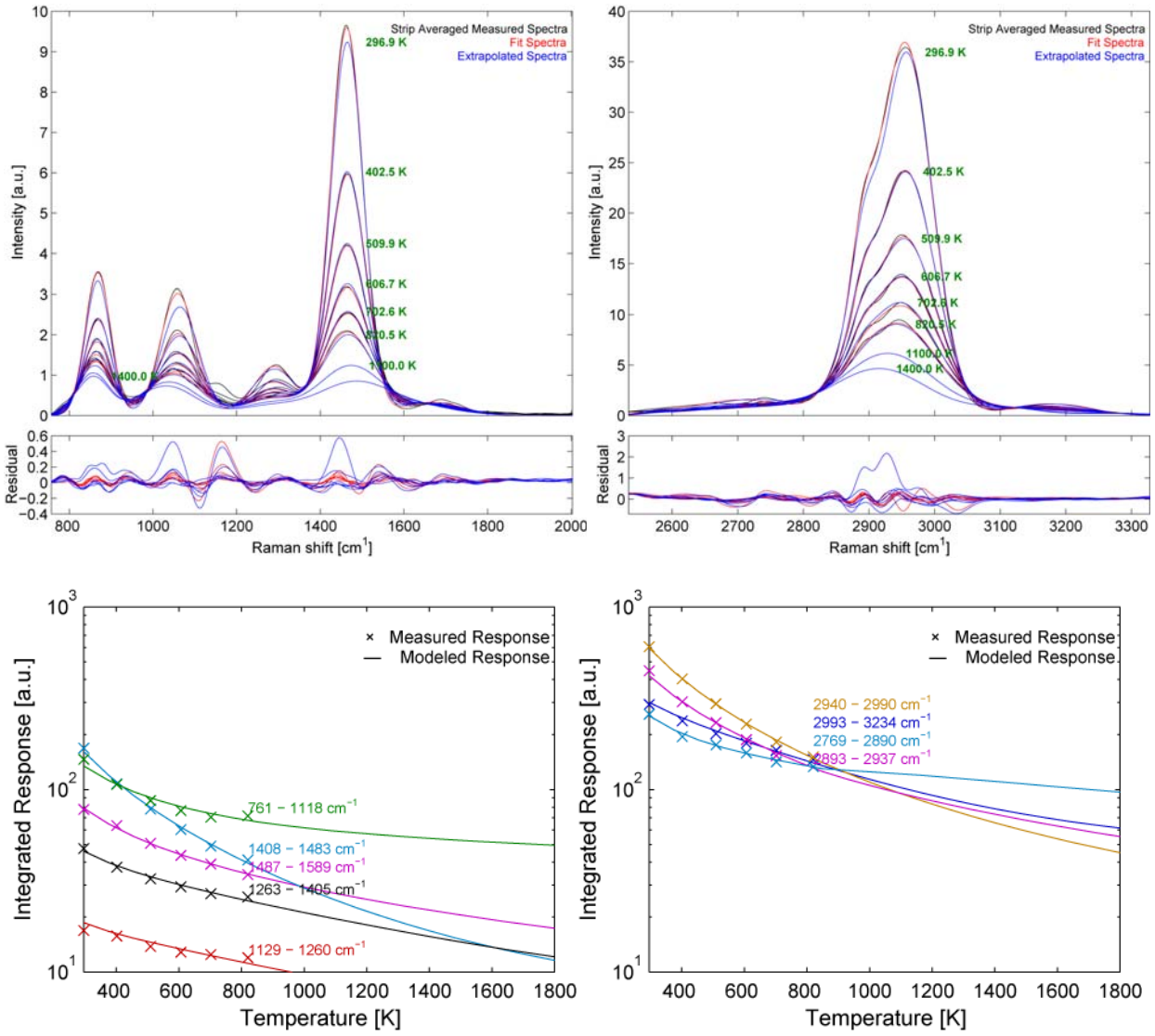

Figure 31. Reference (black), fit (red), and extrapolated (blue) spectra for the p-polarized propane (C_3H_8) Raman spectral data (top), along with the measured (symbols) and modeled (solid line) integrated response (bottom).

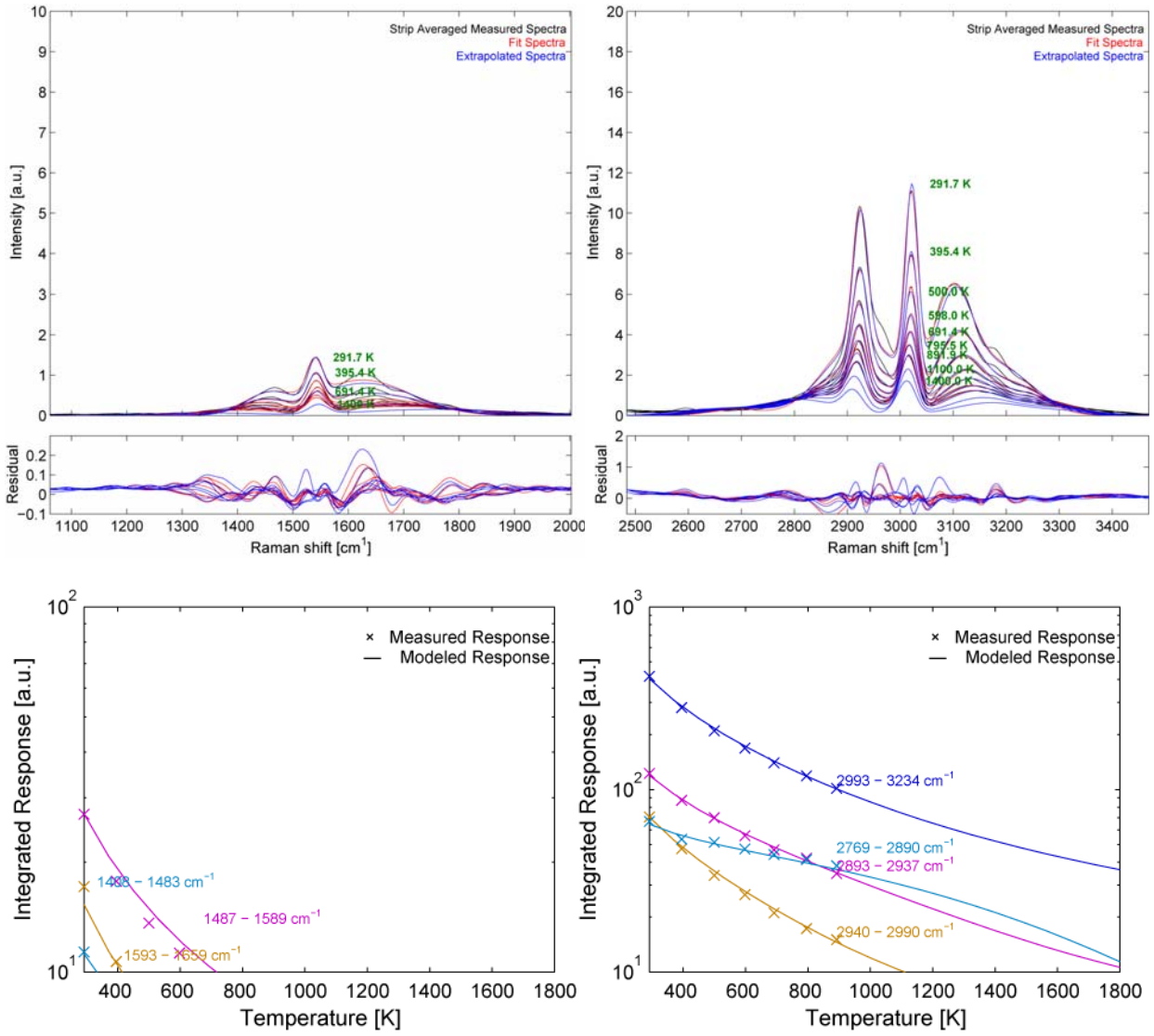

Figure 32. Reference (black), fit (red), and extrapolated (blue) spectra for the p-polarized methane (CH_4) Raman spectral data (top), along with the measured (symbols) and modeled (solid line) integrated response (bottom).

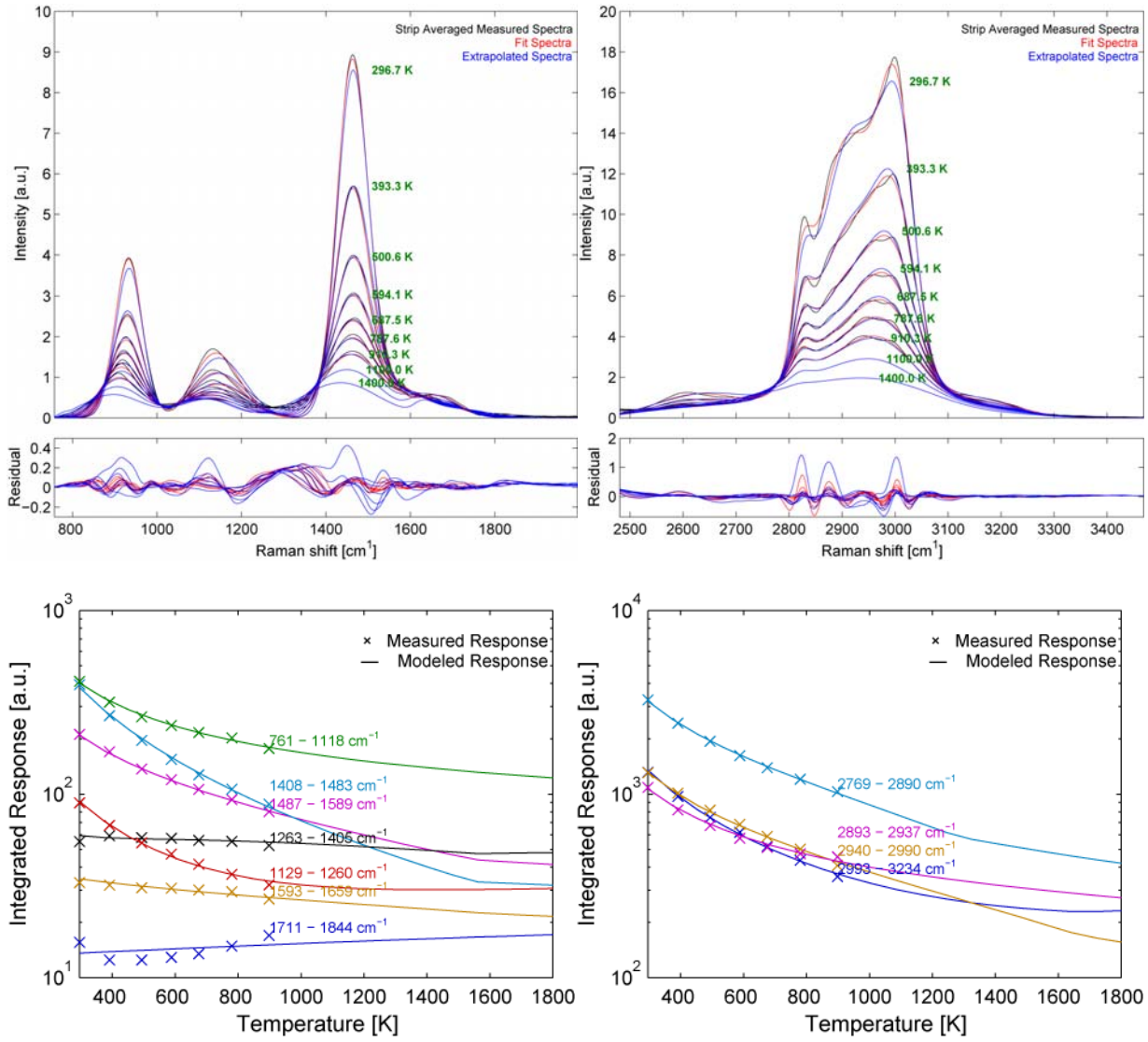

Figure 33. Reference (black), fit (red), and extrapolated (blue) spectra for the p-polarized DME (CH_3OCH_3) Raman spectral data (top), along with the measured (symbols) and modeled (solid line) integrated response (bottom).

DISTRIBUTION

1	MS0899	Technical Library	9536 (electronic copy)
2	MS0359	D. Chavez, LDRD Office	1911
3	MS0115	OFA/NFE Agreements	10012
4	MS0161	Legal Technology Transfer Center	11500
5	MS9051	Robert S. Barlow	8351
6	MS9052	Daniel E. Dedrick	8367
7	MS9052	Isaac W. Ekoto	8367

Sandia National Laboratories